# Quantitative Investigation on the Slip/Twinning Activity and Cracking Behavior During Low-Cycle Fatigue of an Extruded Mg-3Y Sheet

Y.C. DENG, Z.J. HUANG, T.J. LI, D.D. YIN, and J. ZHENG

The slip/twinning activity and cracking behavior of an extruded Mg-3Y sheet during strain-controlled tension-compression low-cycle fatigue (LCF) at room temperature were studied quantitatively and statistically by slip trace analysis and EBSD-based misorientation analysis combined with SEM. The twinned area fraction was 1.7 pct after 200 cycles indicating that twinning contributed limited plastic deformation, and only tension twins were observed. Among 989 grains analyzed, 11.4 pct grains exhibited observable slip traces. Basal slip, with a relative frequency of 81.4 pct, was the dominant deformation mode, and pyramidal II slip (12.4 pct) also exhibited a high activity. The slip-dominated deformation was responsible for the symmetrical hysteresis loops. Among the total 311 cracks observed after 200 cycles, 80.1 pct were intergranular and 19.9 pct were transgranular. The appearance of the two kinds of cracks was closely related. Persistent slip band (PSB, 13.8 pct) and twin (TW, 5.5 pct) were two key transgranular crack initiation sites. The PSB cracking fraction (cracked PSBs/total PSBs) for different slip modes followed pyramidal II (64 pct) > basal (36 pct) > prismatic (14 pct). Strain localization was likely to be responsible for the high cracking fraction of pyramidal II PSBs, which was consistent with their small normalized Schmid factors and the heterogeneous distribution of geometrically necessary dislocation density. Slip/Twinning transfers at grain boundary were also occasionally observed and they were closely associated with transgranular cracks.

## I. INTRODUCTION

MAGNESIUM (Mg) and its alloys, due to their lightweight, high specific strength, high specific stiffness, and good processability, are considered as a new type of lightweight material with great application value and research prospect, which are widely used in structural components of aerospace, high-speed trains, automobile and other fields.[1] The deformation mechanism and cracking behavior of Mg alloys under quasi-static loading have been extensively investigated.[2–5] During actual service, structural components are often subjected to alternate loading (fatigue), and it is well known that materials show significantly different deformation mechanism and cracking behavior during fatigue compared to quasi-static uniaxial loading.[6,7] Therefore, research on the deformation mechanism and cracking behavior of Mg alloys during fatigue is essential. It has been shown that the data obtained from strain-controlled fatigue experiments under fully constrained loading conditions are closer to the actual service conditions.[8] Thus, understanding the deformation mechanism and cracking behavior of Mg alloys during strain-controlled fatigue is critical for regulating the service performance of structural components under alternate loading and accelerate the application of Mg alloys.

Due to the hexagonal close-packed (HCP) crystal structure, Mg alloys have limited deformation modes at room temperature.[9,10] Usually, basal $\langle a \rangle$ slip and $\{10\bar{1}2\} \langle \bar{1}011 \rangle$ tension twinning are the two dominated deformation modes.[11,12] The limited deformation modes together with strong texture formed in thermo-mechanical processing caused strong anisotropy and low ductility of traditional Mg alloys at room

Y.C. DENG, Z.J. HUANG, and D.D. YIN are with the Key Laboratory of Advanced Technologies of Materials, Ministry of Education, School of Materials Science and Engineering, Southwest Jiaotong University, Chengdu, 610031, Sichuan P.R. China. Contact e-mail: ahnydd@swjtu.edu.cn T.J. LI and J. ZHENG are with the International Joint Laboratory for Light Alloys (Ministry of Education), College of Materials Science and Engineering, Chongqing University, Chongqing, 400044, P.R. China. Contact e-mail: jzheng@cqu.edu.cn
Y.C. Deng and Z.J. Huang have contributed equally to this work.
Manuscript submitted August 22, 2020; accepted October 23, 2020.
Article published online November 9, 2020

temperature,[13–15] which hinders their wide application. It has been demonstrated that addition of rare-earth (RE) element yttrium (Y) can greatly influence the deformation mechanism and resultantly alter the deformation behavior and improve the mechanical property of Mg. Lu et al.[16] reported more than 30 pct tensile elongation of the extruded Mg-Y sheets at room temperature. Zhang et al.[17] observed tension-compression yield symmetry in Mg-7.4Y (wt pct) alloy at room temperature. Long et al.[18] investigated the deformation mechanisms of extruded Mg-Y sheets with various Y contents during room temperature compression. They found that Y can remarkably restrain twinning and promote pyramidal slip. Sandlöbes et al.[19] found that the Y enhanced the $\langle c + a \rangle$ slip of Mg-Y sheets during rolling at room temperature, which improved the formability of Mg.

However, the above studies of deformation mechanisms are mainly based on quasi-static uniaxial loading. Great efforts have been made to understand the fatigue behavior of Mg-RE alloys, which mainly focus on the cracking behavior rather than the deformation mechanisms.[20–23] For example, Yue et al.[20] studied the high-cycle fatigue (HCF) deformation of cast NZ30K alloys at room temperature, and they found that there were two typical damage morphologies: one was persistent slip band (PSB) crack formed by the cumulation of slip, the other was intragranular cracks formed by twin boundary (TB). Compared to the cracking behavior, little work has been done to understand the deformation mechanism during fatigue. Huo et al.[24] studied the morphology of slip traces and the active twin types for Mg-2.2Y alloy during cyclic tension deformation at room temperature. However, they did not identify the active slip systems. What's more, the PSB is a critical crack initiation site as mentioned above, but what kind of PSBs induced by various slip modes are more likely to crack is an interesting topic and needs to be clarified. This problem is particularly important for Mg-RE alloys since RE alloying can enhance the non-basal slip activity, which can hardly be activated in conventional Mg alloys.[17,19,25] Up to now, the deformation mechanisms and their correlation to the cracking behavior of Mg-RE alloys during fatigue are still lacking.

In the current work, we performed a quantitative investigation on the slip/twinning activity and cracking behavior of an extruded Mg-3Y sheet under strain-controlled tension-compression low-cycle fatigue (LCF) at room temperature. The grain-scale slip trace analysis and grain boundary misorientation analysis were used to obtain quantitative and statistical activities of various slip modes and to identify twinning activity, respectively. The onset of different slip modes and cracks was identified by tracking the same area during the cyclic deformation. The correlation between macroscopic stress-strain response and slip/twinning activity as well as the relation of deformation modes and cracking behavior was discussed. This study can provide insights into the fatigue of Mg-RE alloys, and the quantitative and statistical information about the operating deformation mechanisms and cracking patterns is valuable for simulation and modeling.

## II. EXPERIMENTAL PROCEDURES

The material with a nominal composition of Mg-3Y (wt pct, hereafter, all alloy compositions are in weight percent unless otherwise stated) was prepared by melting high-purity Mg ($\geq$ 99.9 pct) and Mg-30Y master alloys, and then extruded to the sheet with a cross-section of $80 \times 5$ mm$^2$. The details of casting and extrusion process can be found in our previous studies.[26] The actual composition of the Mg-3Y sheet is Mg-2.7Y, measured by an inductively coupled plasma (ICP) analyzer (Perkin Elmer, Plasma 400).

Dog-bone shaped samples with a gauge length of 8 mm (parallel to the extrusion direction, ED), a width of 4.5 mm (parallel to the transverse direction, TD), and a thickness of 4.0 mm (parallel to normal direction, ND) were cut by electric spark machining from the extruded sheets.

The LCF experiments of Mg-3Y alloy were performed under strain-controlled tension-compression loading at room temperature using a biaxial hydraulic-servo testing machine (MTS 809 Axial/Torsional) equipped with an extensometer (Epsilon 3442-008M-020M-ST). The fatigue test conditions consisted of a strain ratio of $R = -1$, and loading was started with tension along the ED. A constant strain amplitude (1 pct) was employed, and the corresponding frequency was 0.1 Hz. All the fatigue tests were conducted until the stress amplitude decreased over 5 pct, which the corresponding cycle is considered as the fatigue failure cycle, i.e., the fatigue life.[27]

Prior to testing the sample surface was prepared for electron backscatter diffraction (EBSD) analysis using standard mechanical polishing followed by electropolish in an AC$_2$ solution at $-$ 20 °C and a voltage of 20 V, a current of 0.1 to 0.2 A for ~ 2 minutes. Microstructure and crystallographic orientation observations were performed by field emission scanning electron microscopes (SEM, Zeiss Auriga SEM-FIB or JEOL JSM-7800F) and EBSD detector (Oxford Nordlys F) inside the SEM chamber, respectively. All characterizations were carried out in ED-TD plane. To maximize the EBSD signal, an acceleration voltage of 20 kV, a working distance of 10 mm, and a sample tilt angle of 70 deg were selected. The step size (0.35 $\mu$m) was selected for both fine resolution and enough grains (~ 1000). The quasi-in-situ fatigue experiment was interrupted to perform SEM and EBSD observations for the same area with fiducial markers at 1 pct tensile strain of the selected loading cycles (i.e., before loading, 1st cycle, 10th cycle, 50 and 100 pct of fatigue failure cycle). However, due to the low indexing rate (65 pct) caused by strain accumulation, the sample after the fatigue failure cycle was re-polished for better EBSD observation. Thus, the EBSD scan area for the fatigue failure cycle is no longer quasi-in-situ. The EBSD indexing rates for all the EBSD data used in this study are at least 90 pct.

A home-made MATLAB code based on the open-source toolbox MTEX[28,29] was used to analyze the EBSD orientation data. Grain-scale slip and twinning activities were evaluated by slip trace analysis and twin boundary misorientation analysis, respectively. The

active slip systems of the slip traces observed by SEM image were considered to be the best match to the possible slip traces calculated by the home-made MATLAB code, which used the grain mean orientation obtained by EBSD before loading. Details of the slip trace analysis can be found in previous work.[18,30–32] Twinning plane trace analysis, which is similar to the above slip trace analysis, was also adopted for twinning system identification if the EBSD indexing rate was low due to strain accumulation.

## III. RESULTS

### A. Initial Microstructure

Figure 1 illustrates representative microstructure and texture characteristics for the as-extruded Mg-3Y sheet in the ED-TD plane. As shown in Figures 1(a) and (b), the as-extruded microstructure was fully recrystallized with uniform fine equiaxed grains, and the average equivalent grain diameter was $7.1 \pm 3.7\ \mu m$. There were some negligible second-phase particles and details of this phase can be found in our previous studies.[16,26] The high-angle grain boundaries (> 10 deg) accounted for about 96 pct, which confirmed the fully recrystallized microstructure. It should be noted that the microstructure before loading was twin free. Figure 1(e) shows the {0001} pole figure (PF). The maximum basal pole spread in TD and split into two lobes in ED with a maximum intensity of 7.2 mrd, which tilted ~ 30 to 45 deg from ND toward to ED. As shown in the inverse pole figure (IPF), the sheet exhibited a main peak around $\langle 11\bar{2}1 \rangle$ indicating that the $\langle 11\bar{2}1 \rangle$ directions of most grains were nearly parallel to the ED. The above texture characteristics are typical rare-earth texture features.[17, 29]

### B. Cyclic Mechanical Behavior

In the current study, fatigue life (fatigue failure cycle) is defined as the cycle in which stress amplitude decreased by 5 pct, and the cycle at which the specimens reached 50 pct of the fatigue life is defined as the stable cycle.[33] The fatigue life was identified to be the 200th cycle for the present Mg-3Y sheet. Hereafter, the corresponding half-life cycle was the 100th cycle (the stable cycle). In a stress cycle, peak stress ($\sigma_{max}$) and valley stress ($\sigma_{min}$) was the maximum stress in tensile and compressive reversals, respectively. Stress amplitude ($\Delta\sigma/2$) and mean stress ($\sigma_{m}$) are defined as follows:

$$\Delta\sigma/2 = \frac{\sigma_{max} - \sigma_{min}}{2} \qquad [1]$$

$$\sigma_{m} = \frac{\sigma_{max} + \sigma_{min}}{2} \qquad [2]$$

Figure 2 presents the cyclic mechanical behavior obtained from the strain-controlled LCF tests of Mg-3Y with 1 pct strain amplitude. The evolution of
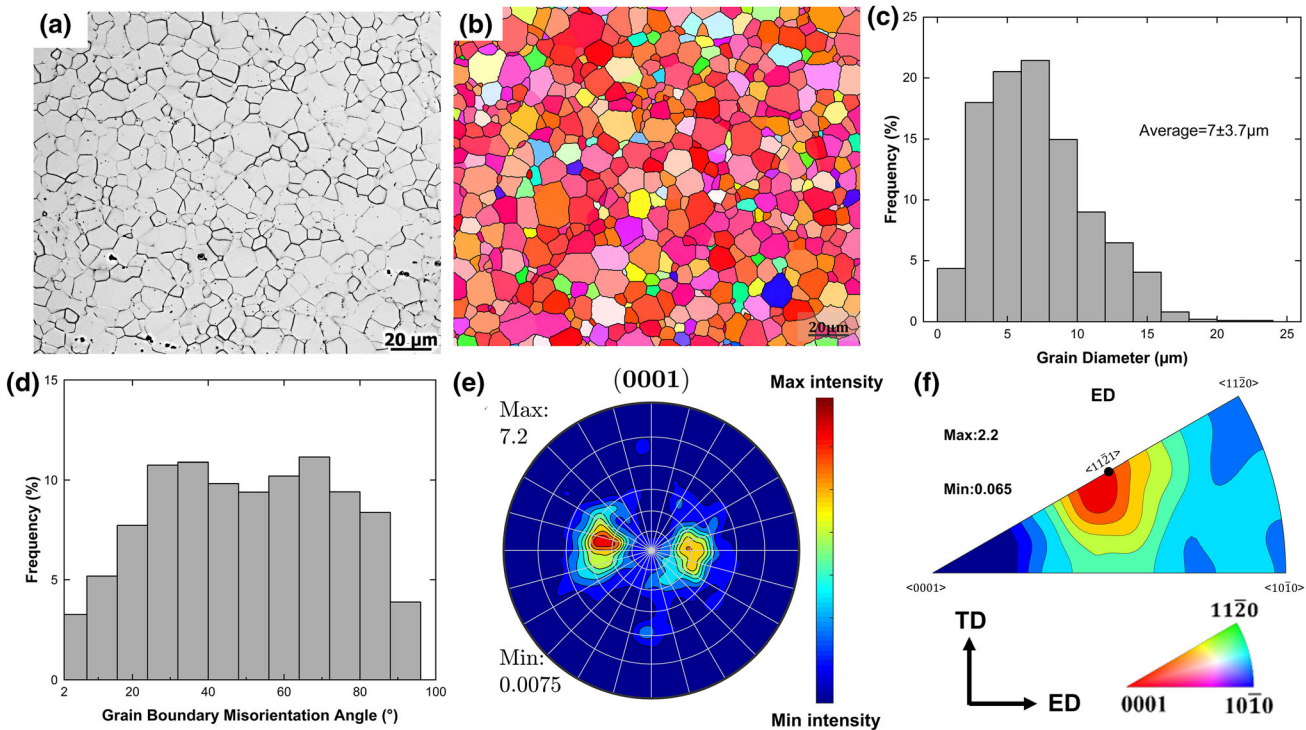


Fig. 1—Representative microstructure and texture characteristics of the as-extruded Mg-3Y sheet for the ED (extrusion direction)-TD (transverse direction) plane: (a) optical microscopy image, (b) IPF map along the normal direction (ND), (c) equivalent grain diameter distribution, (d) grain boundary misorientation angle distribution, (e) the {0001} pole figure (PF), and (f) the inverse pole figure (IPF) for ED. Note that unless otherwise stated, all the observations in this work were made in the ED-TD plane.
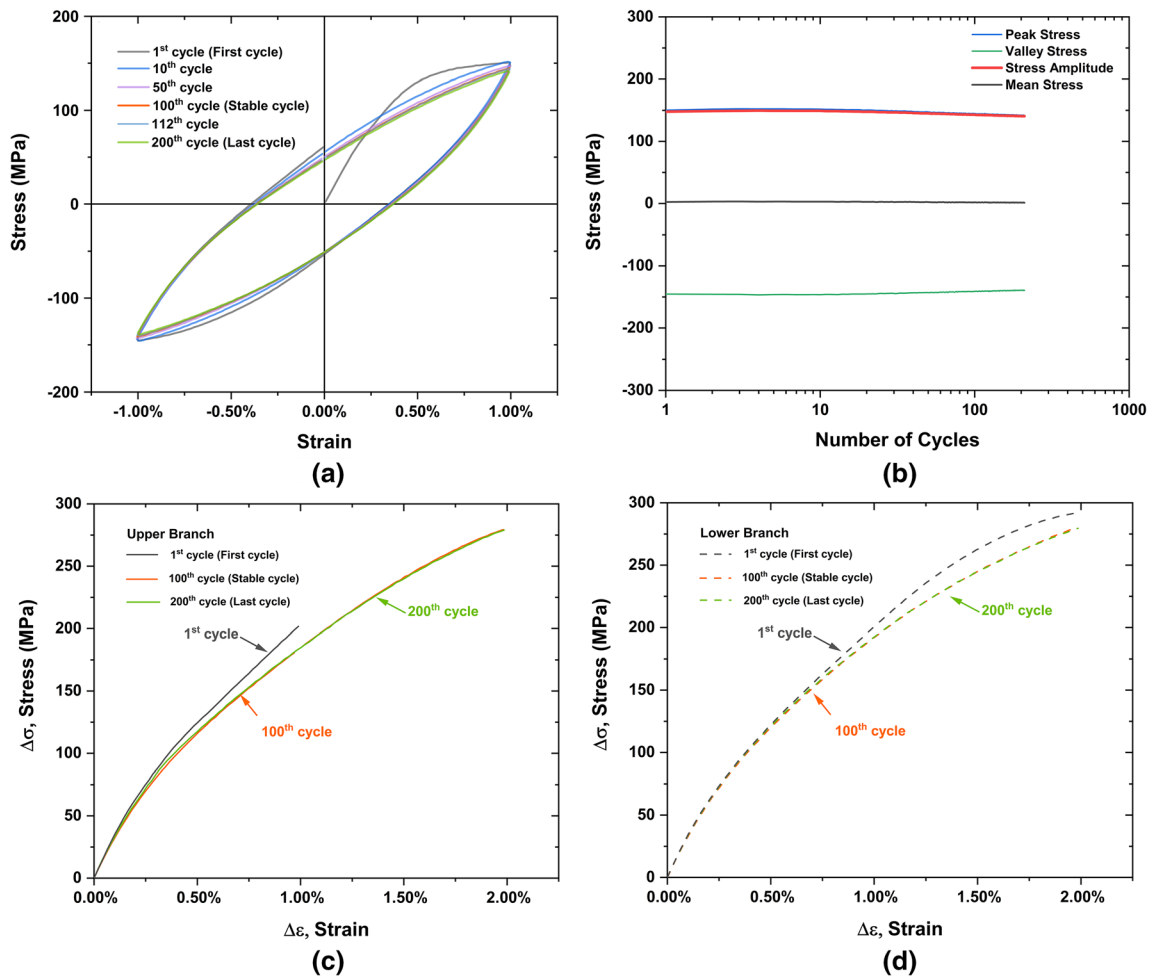
Fig. 2—(*a*) Evolution of stress-strain hysteresis loops of the samples during 1 pct strain amplitude LCF test, (*b*) evolution of peak stress, valley stress, mean stress, and stress amplitude as a function of cycles, stress-strain responses of the (*c*) upper branch, and (*d*) lower branch for the representative cycles.

typical stress–strain hysteresis loops during the deformation is provided in Figure 2(a). During the cyclic loading, the shape of stress–strain hysteresis loops of tensile and compressive reversals was symmetric, which is different from the asymmetric hysteresis loops of conventional Mg alloys.[34–37] With increasing cycles, the shape of the stress–strain hysteresis loops remained almost stable until the last cycle (the 200th cycle). Figure 2(b) illustrates the peak stress, valley stress, stress amplitude, and mean stress as a function of cycles. The peak stress slightly increased during the first four cycles and then declined slowly with increasing cycles. Similar trends for the valley stress and stress amplitude were observed during the deformation. For example, the stress amplitude increased from 147.8 MPa (the 1st cycle) to 149.5 MPa (the 4th cycle), and then declined slowly. Similar cyclic hardening first and then softening were also observed in extruded Mg-Y-Gd alloys during strain-controlled tension-compression fatigue.[27] The

mean stress remained around zero during the cyclic deformation was consistent with the symmetric stress–strain hysteresis loops.

To further study the plastic deformation during the LCF, the stress–strain hysteresis loops were divided into two parts: the upper branch and the lower branch. The upper branch means a load process that started with 1 pct compressive strain ($\varepsilon_{min}$), followed by unloading and tensile loaded to 1 pct tensile strain ($\varepsilon_{max}$). The lower branch represents a deformation process, which started with $\varepsilon_{max}$, followed by unloading and compressively loaded to $\varepsilon_{min}$. By coordinate transformation (for upper branch: $\Delta\sigma = \sigma - \sigma_{min}$, $\Delta\varepsilon = \varepsilon - \varepsilon_{min}$; for lower branch: $\Delta\sigma = \sigma_{max} - \sigma$, $\Delta\varepsilon = \varepsilon_{max} - \varepsilon$),[36] the upper branches and lower branches of the typical cycles are provided in Figures 2(c) and (d), respectively. The $\Delta\sigma - \Delta\varepsilon$ curves of the upper branches and the lower branches for various cycles were almost symmetric (the upper branch of the first cycle was only half of that for the

lower branch because of the test starting with tensile loading). The upper branch shapes of the stable cycle and last cycle (Figure 2(c)) were almost identical, and a similar trend was found in the lower branches (Figure 2(d)). What's more, both the upper branches and lower branches showed a concave-down shape indicating slip-dominated deformation, which will be confirmed and discussed in Section IV–A. In a word, the characteristics of the upper and lower branches are consistent with the symmetric and stable stress–strain hysteresis loops and further confirmed the Mg-3Y sheet exhibited symmetric cyclic deformation behavior during the LCF.

## C. Microstructural Evolution During the LCF

In order to understand the underlying deformation mechanisms for the macroscopic stress–strain response during the cyclic tension-compression deformation, detailed microstructural evolution investigations, with special attention on slip activity, twinning activity, deformation inhomogeneity and fatigue damage morphologies at grain-scale, were performed by tracking the same area on the sample surface. No observable slip traces appeared at the maximum tensile strain ($\varepsilon_{max}$, all the observations were made at this point) of the 1st and 10th cycles, so we jumped to the 100th cycle (the stable cycle) and the 200th cycle (the last cycle) to perform the observations.

### 1. Slip activity

Figure 3 illustrates the representative microstructure characteristic evolution of the sheet for the same area during the LCF. A few slip traces were observed firstly at the 100th cycle (the stable cycle), and they increased with increasing cycles. Among 989 grains examined, 2.0 pct (20) and 11.4 pct (113) grains exhibiting observable slip traces for the 100th cycle (the stable cycle) and the 200th cycle (the last cycle), respectively. The slip traces exhibited typical characteristics of planar slip (i.e., long and straight slip lines paralleling to each other). Usually, one grain exhibited one set of parallel slip traces indicating that single slip dominated the deformation.

Some cracks were also found in the figure since the 100th cycle (the stable cycle), and the details of the cracking behavior will be provided in Section III–D.

The quantitative and statistical slip trace analysis was inducted to identify the active slip systems corresponding to the observed slip traces grain by grain. The following 3 slip modes corresponding 12 slip systems were considered[38]:

1. $\{0001\}\langle11\bar{2}0\rangle$: Basal $\langle a\rangle$;
2. $\{10\bar{1}0\}\langle11\bar{2}0\rangle$: First-order prismatic $\langle a\rangle$;
3. $\{11\bar{2}2\}\langle\bar{1}\bar{1}23\rangle$: Second-order pyramidal $\langle c + a\rangle$.

Figure 4 shows an example of the active slip system identification in grain 331 for the sample fatigue tested to the 200th cycle (the last cycle) by the slip trace analysis. One series of slip traces was observed by SEM in this grain, as shown in Figure 4(a). The orientation corresponding to the grain was also visualized (Figure 4(b)). All possible slip plane traces together with slip systems (Figure 4(c)) were calculated by the home-made MATLAB code using the undeformed grain mean orientation. In terms of the best match between the calculated and the observed slip traces, the slip system 3, with the highest Schmid factor $m$ (0.42) compared with slip system 1 and 2, was considered as the appropriate active slip system, which belongs to basal $\langle a\rangle$ slip.

Using the above method, the active slip systems in ~ 113 grains were determined for the sample fatigue tested to the 200th cycle (the last cycle). Most of the active slip systems were identified unambiguously base on distinct slip plane traces and reasonable deviation angles. However, if more than one slip systems share the same slip plane (this only happens in basal $\langle a\rangle$ slip), the slip system with the highest $m$ was considered as the activated one.[31]

In addition, there were 7 pairs of slip transfer across grain boundary in the studied area, and they were all observed in the 200th cycle (the last cycle). Dislocations might transfer across grain boundary when they encounter the grain boundary, and continue to slip with the same slip system or not.[39] Thus, slip traces might be observed at both sides of grain boundary. Besides,
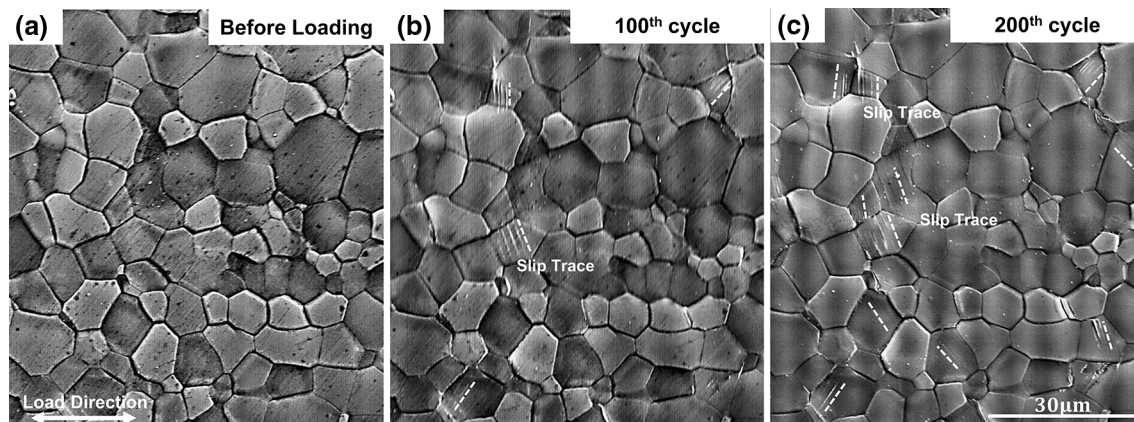


Fig. 3—Sequential SE SEM photomicrographs illustrating the representative microstructural evolution of the samples during the LCF deformation: (a) to (c) showing prevalent slip traces marked by white dashed lines. The associated number of cycles is indicated in the images.
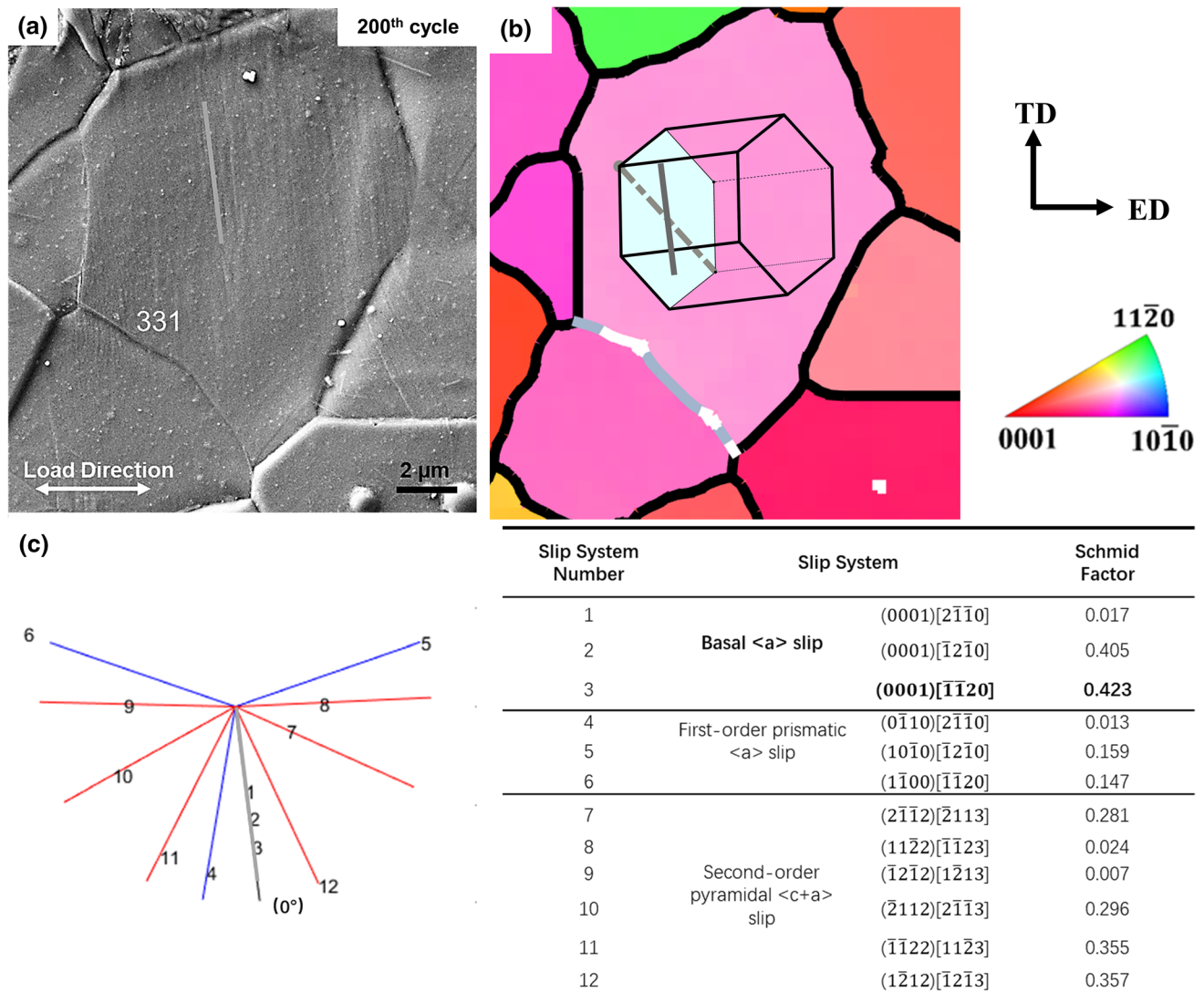
| Slip System Number | Slip System | | Schmid Factor |
|---|---|---|---|
| 1 | | $(0001)[2\bar{1}\bar{1}0]$ | 0.017 |
| 2 | Basal <a> slip | $(0001)[\bar{1}2\bar{1}0]$ | 0.405 |
| 3 | | $\mathbf{(0001)[\bar{1}\bar{1}20]}$ | **0.423** |
| 4 | First-order prismatic <a> slip | $(0\bar{1}10)[2\bar{1}\bar{1}0]$ | 0.013 |
| 5 | | $(10\bar{1}0)[\bar{1}2\bar{1}0]$ | 0.159 |
| 6 | | $(1\bar{1}00)[\bar{1}\bar{1}20]$ | 0.147 |
| 7 | | $(2\bar{1}\bar{1}2)[\bar{2}113]$ | 0.281 |
| 8 | | $(11\bar{2}2)[\bar{1}\bar{1}23]$ | 0.024 |
| 9 | Second-order pyramidal <c+a> slip | $(\bar{1}2\bar{1}2)[1\bar{2}13]$ | 0.007 |
| 10 | | $(\bar{2}112)[2\bar{1}\bar{1}3]$ | 0.296 |
| 11 | | $(\bar{1}\bar{1}22)[11\bar{2}3]$ | 0.355 |
| 12 | | $(1\bar{2}12)[\bar{1}2\bar{1}3]$ | 0.357 |

Fig. 4—An illustration of slip trace analysis performed on the grain 331 in the sample tested to the 200th cycle: (*a*) SE SEM photomicrograph and (*b*) the corresponding IPF map along the ND obtained before deformation. The grain orientation is visualized by HCP unit cell (light blue shaded plane, grey dashed line, and solid grey line represents the slip plane, slip direction and slip plane trace, respectively) and details of the 12 possible slip systems which were calculated based on EBSD orientation data are exhibited in (*c*), including slip system, slip plane, slip direction, and corresponding Schmid factor *m*. The slip system 3 was chosen as the appropriate active slip system according to the best match between the calculated traces and the observed traces. The deviation angle from the identified trace to the observed slip trace is also shown in parentheses (Color figure online).

similar transfer behavior may occur for twinning. 2 pairs of twinning transfer across grain boundary were observed in the 200th cycle (the last cycle). One of the critical parameters for evaluating the ease of slip/twinning transfer, the Luster–Morris $m'$ parameter also as known as the geometric compatibility parameter, can be defined below.[40]

$$m' = \cos \psi \cos \kappa \qquad [3]$$

where $\psi$ is the angle between the two slip/twinning plane normals, and $\kappa$ is the angle between the Burgers vectors/twinning directions for the involved two slip/twinning systems. The closer the $m'$ to 1 (possible maximum value), the more geometrically compatible for the involved slip/twinning systems are, consequently the transfer is more likely accessible.

Figure 5 illustrates an example of slip transfer across the grain boundary for grain pair 266 to 290. The active slip systems were identified as the same slip system 2 (basal $\langle a \rangle$ $(0001)[\bar{1}2\bar{1}0]$) but with slightly different $m$ values of 0.41 and 0.42 for the two transferred slip systems. The corresponding $m'$ value was as high as 0.97. Details of all the slip/twinning transfer pairs are provided in Table I. Most of the $m'$ values were above 0.7.

Figure 6 summarizes the Schmid factor, normalized Schmid factor distributions, and the frequency of the identified slip traces for a particular slip mode. Overall, a similar trend was observed for both the 100th (the
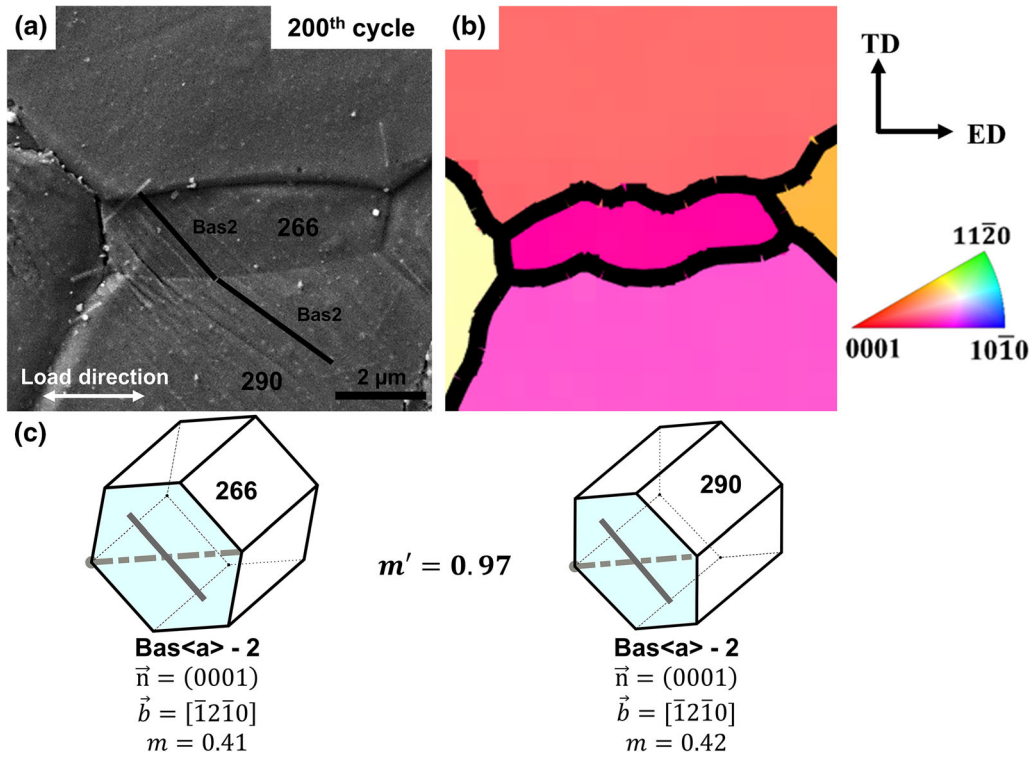
Fig. 5—An example showing slip transfer across grain boundary in the sample tested to the 200th cycle: (*a*) SE SEM photomicrograph , (*b*) the corresponding IPF map along the ND obtained before deformation, and (*c*) visualization of the identified active slip systems and grain orientation in the HCP unit cells for the two grains. The slip system, Schmid factor *m*, and Luster–Morris parameter *m'* are also indicated in the images.

**Table I. Details of Slip/Twinning Transfer Pairs Across Grain Boundary**

| | Grain1 | Grain2 | Slip/Twinning Plane1 | Slip/Twinning Plane2 | Slip/Twinning Direction1 | Slip/Twinning Direction2 | $m1$ | $m2$ | $m'$ |
|---|---|---|---|---|---|---|---|---|---|
| Slip | 49 | 101 | (0001) | (0001) | $[\bar{1}2\bar{1}0]$ | $[\bar{1}2\bar{1}0]$ | 0.46 | 0.44 | 0.84 |
| | 51 | 54 | (0001) | (0001) | $[\bar{1}2\bar{1}0]$ | $[\bar{1}2\bar{1}0]$ | 0.44 | 0.40 | 0.95 |
| | 51 | 63 | (0001) | $(\bar{1}\bar{1}22)$ | $[\bar{1}2\bar{1}0]$ | $[11\bar{2}3]$ | 0.44 | 0.36 | 0.16 |
| | 78 | 101 | (0001) | (0001) | $[\bar{1}\bar{1}20]$ | $[\bar{1}2\bar{1}0]$ | 0.45 | 0.44 | 0.05 |
| | 266 | 290 | (0001) | (0001) | $[\bar{1}2\bar{1}0]$ | $[\bar{1}2\bar{1}0]$ | 0.41 | 0.42 | 0.97 |
| | 815 | 838 | (0001) | (0001) | $[\bar{1}2\bar{1}0]$ | $[\bar{1}\bar{1}20]$ | 0.47 | 0.47 | 0.68 |
| | 887 | 915 | (0001) | (0001) | $[\bar{1}\bar{1}20]$ | $[\bar{1}\bar{1}20]$ | 0.48 | 0.46 | 0.87 |
| Twinning | 290 | 320 | $(\bar{1}012)$ | $(\bar{1}102)$ | $[10\bar{1}1]$ | $[1\bar{1}01]$ | 0.08 | 0.07 | 0.76 |
| | 777 | 796 | $(1\bar{1}02)$ | $(1\bar{1}02)$ | $[\bar{1}101]$ | $[\bar{1}101]$ | 0.45 | 0.47 | 0.96 |

*Note* Twinning's Schmid factor takes the absolute value.

stable cycle) and the 200th (the last cycle) cycles, but the slip activity was higher for the 200th cycle, especially for the non-basal slips, as shown in Figure 6(a). Among the 113 identified active slip systems, basal ⟨a⟩ slip was predominant accounted for 81.4 pct, and 2nd pyramidal ⟨c + a⟩ slip (12.4 pct) was much more active than prismatic ⟨a⟩ slip (6.2 pct). The slip systems with larger *m* values seemed to be more active, which was consistent with the Schmid's law. However, non-negligible slip systems with small *m* values (0 to 0.1) were also activated, and they were usually observed for the non-basal slips.

In order to further investigate the above phenomenon, the Schmid factor (*m*) of the operating non-basal slip system was normalized as follows:

$$m_{nor} = \frac{m - m_{min}}{2(m_{max} - m_{min})} \qquad [4]$$

The value of normalized Schmid factor ($m_{nor}$) represents how the *m* close to the possible maximum Schmid factor, $m_{max}$, in the same slip mode. Larger $m_{nor}$ means the corresponding active *m* is closer to the possible $m_{max}$. As shown in Figure 6(b), the $m_{nor}$ tended to distribute at either large values ($m_{nor} > 0.3$, ∼ 61.9 pct) or small
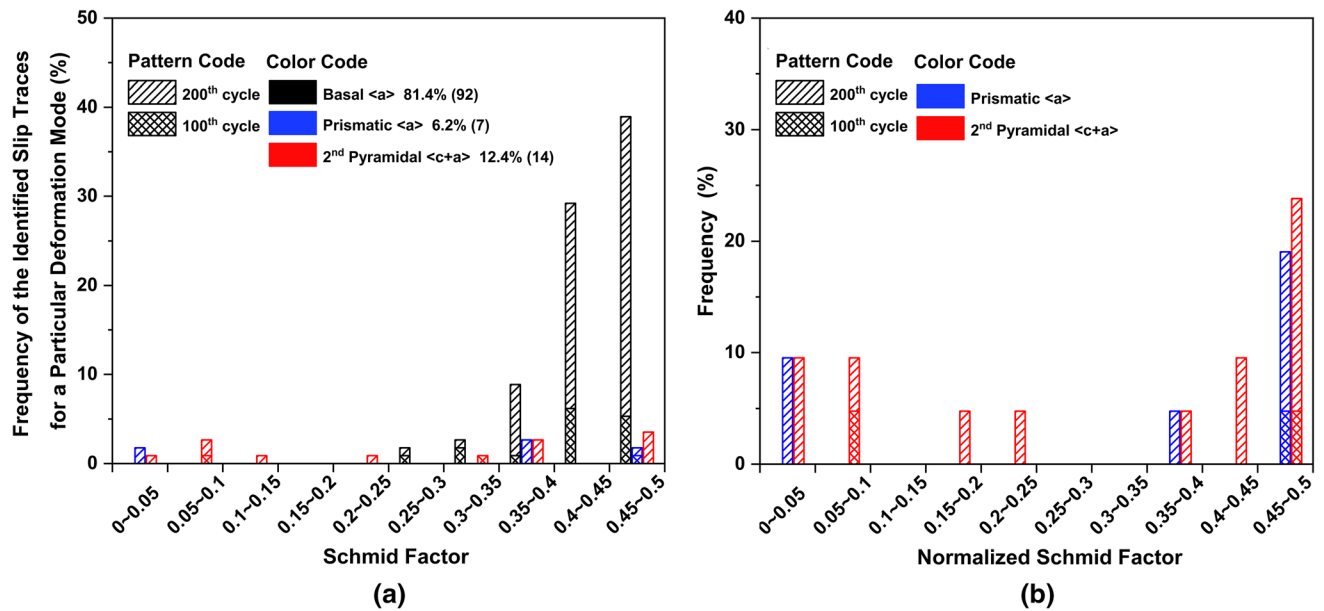
Fig. 6—(a) Schmid factor (*m*) and (b) normalized Schmid factor ($m_{nor}$) distributions of the identified slip traces for a particular slip mode in the specimen tested to different cycles. The number in parentheses represents the total number of grains exhibiting slip traces.

values ($m_{nor} < 0.1$, ~ 28.6 pct) for the two non-basal slip modes. Moreover, the $m_{nor}$ distribution for 2nd pyramidal $\langle c + a \rangle$ was more dispersed compared with that of prismatic $\langle a \rangle$ slip. The above results suggested that the variant selection of slip system mainly responded to global stress, but the local stress concentration was also expected to play a critical role in activating non-basal slip modes.

Figure 7 illustrates the distribution of the deviation angles of the identified slip traces from their best match calculated traces for all the ~ 113 grains exhibiting observable slip traces. All the deviation angles were below 8 deg, and most of them (90 pct) were within 6 deg. The possible reasons for this deviation may be related to the deformation-induced lattice rotation and the misalignment of the SEM/EBSD system.

### 2. Twinning activity

As deformation increasing, strain may accumulate in the material accompanying relief at the sample surface, which will damage the EBSD pattern quality and associated indexing. Therefore, the sample experienced 200 cycles LCF was slightly re-polished for obtaining good EBSD results. Boundary misorientation analysis was performed to identify different twin modes based on misorientation angle/axis relationship of twin and parent. According to the literature,[40] five twin modes with the corresponding misorientation angle/axis as shown below were considered in this work:

1. $\{10\bar{1}2\}$ tension twin (TTW): 86 deg/$\langle 1\bar{2}10 \rangle$;
2. $\{10\bar{1}1\}$ contraction twin (CTW): 56 deg/$\langle 1\bar{2}10 \rangle$;
3. $\{10\bar{1}3\}$ CTW: 64 deg/$\langle 1\bar{2}10 \rangle$;
4. $\{10\bar{1}1\} - \{10\bar{1}2\}$ double twin (DTW): 38 deg/$\langle 1\bar{2}10 \rangle$;
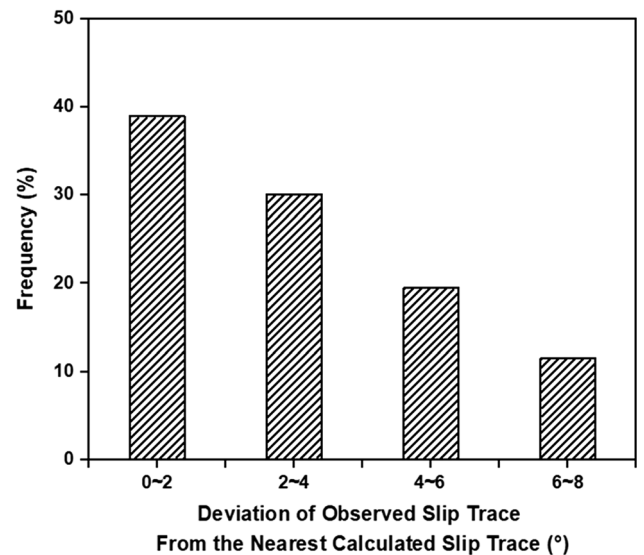5. $\{10\bar{1}3\} - \{10\bar{1}2\}$ DTW: 22 deg/$\langle 1\bar{2}10 \rangle$.



Fig. 7—The deviation angle distribution of the identified slip traces from their best match traces for all the ~ 113 grains in which slip traces were observed in this study.

Figure 8 shows the IPF map and corresponding twin boundaries map for the sample tested to the 200th cycle (the last cycle). Note that the microstructure was twin free before loading, as shown in Figure 1(b). Some thin lenticular twins were observed in the studied area, and all of them were identified as TTWs.

Figure 9 summarizes the statistical information of twin morphology for the TTWs in the sample. 84 TTWs in total 1836 grains, corresponding to 0.05 twins per grain and 1.7 pct twin area fraction, were observed in the studied area. 90 pct of the twin areas was below 50 $\mu m^2$. The average twin thickness and length were
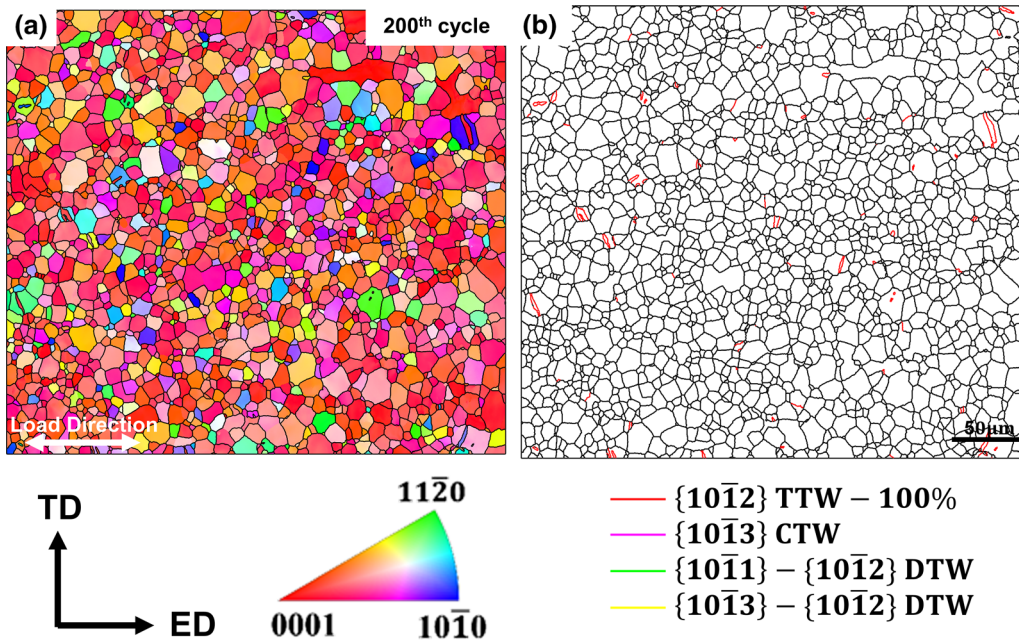
Fig. 8—The (*a*) IPF map along ND and (*b*) the corresponding twin boundaries map for the sample tested to the 200th cycle. The black line represents the high-angle (> 10 deg) grain boundary, and the colored lines represent the boundaries for various twin modes. The relative twin boundary fraction for a particular twin mode with respect to the total twin boundaries are also indicated in the figure (Color figure online).
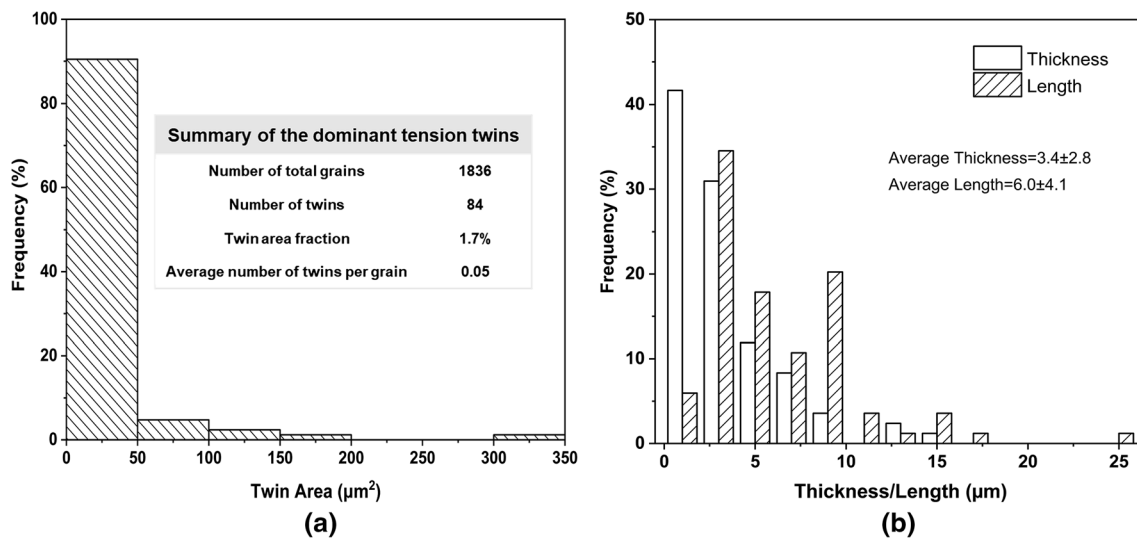


Fig. 9—The statistical information of twin morphology for the TTWs in the sample tested to the 200th cycle: (*a*) the twin area distribution with inserted summary of the dominant TTWs and (*b*) the thickness and length distribution.

$3.4 \pm 2.8$ and $6.0 \pm 4.1$ $\mu$m, respectively. Thus, it is reasonable to conclude that twinning activity was limited during the LCF, and dislocation slip was the dominant deformation mechanism. This is consistent with the symmetric stress–strain hysteresis loops, as shown in Figure 2(a).

3. *Deformation inhomogeneity*

The intragranular misorientation angle (IGM) in a grain is the misorientation angle between the measured point and the grain average orientation, reflecting deformation-induced long-range orientation gradients in a grain.[41] The IGM calculation was based on the EBSD data using MTEX-based home-made MATLAB code. The IGM maps and corresponding histograms before and after 200 cycles LCF are provided in Figure 10. As shown in Figure 10, the IGM increased significantly after 200 cycles deformation. The IGM in most grains were low and showed a uniform distribution in the initial state. After the deformation, more localized areas with high IGM appeared either at the vicinity of grain boundary or in grain interior (Figure 10(c)), and the average IGM for the whole area increased from 0.5 to 1.2 deg with 140 pct increasing rate (Figure 10(d)).
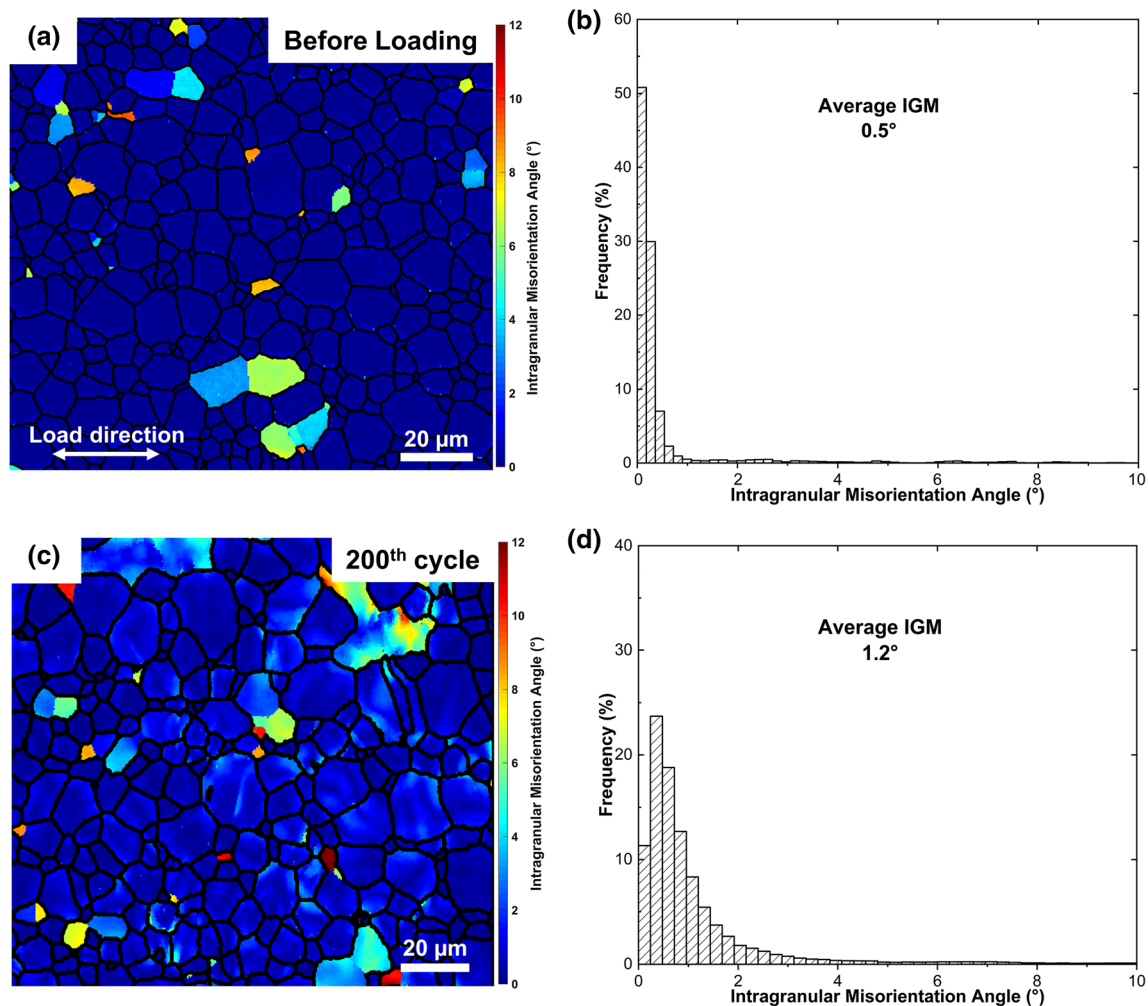
Fig. 10—Intragranular misorientation angle (IGM) maps with corresponding histograms for the sample: (*a*) through (*b*) before loading, and (*c*) through (*d*) tested to the 200th cycle.

The IGM analysis indicates that significant intragranular deformation heterogeneity developed after the deformation.

The geometrically necessary dislocation (GND) represents an extra storage of dislocations to accommodate the strain gradient during non-uniform plastic deformation.[26] The calculation of GND density depends on the active dislocation types.[42] Based on the slip trace analysis in Section III–C–1, the identified 12 slip systems, including basal $\langle a \rangle$ slip, first-order prismatic $\langle a \rangle$ slip and second-order pyramidal $\langle c + a \rangle$ slip, corresponding to 21 dislocation types (12 edge + 9 screw) were considered in the GND calculation. Based on the Nye's dislocation tensor, the GND density was calculated using MTEX based home-made MATLAB code.[41,42] GND density maps with corresponding histograms before and after 200 cycles LCF are provided in Figure 11. The GND density increased remarkably after 200 cycles LCF. Before loading (Figure 11(a)), most grains showed a uniform and relatively low GND densities except that a few high density areas concentrated at the grain boundaries. After the deformation (Figure 11(c)), abundant thin

banded high GND density areas appeared in grain interiors, accompanying by a significant increasing density with 64 pct increasing rate (Figure 11(d)). Note that the high GND density areas were also observed in the vicinity of some grain boundaries. According to the GND analysis results, it is obvious that heterogeneous deformation developed during the LCF.

### D. Cracking Behavior

#### 1. Fatigue crack morphology

From the 100th cycle (the stable cycle) to the 200th cycle (the last cycle), the number of intergranular cracks increased from 236 to 249, and the number of transgranular cracks increased from 57 to 62. It means that most cracks formed within the first 100 cycles. Meanwhile, two "Other" cracks, which are some kinds of transgranular cracks that cannot be reasonably explained at present, were observed.

Figure 12 illustrates various representative types of fatigue crack morphology observed on the sample surface after the 200th cycle, mainly including intergranular cracks (marked by crack 1, 2 and 3), persistent
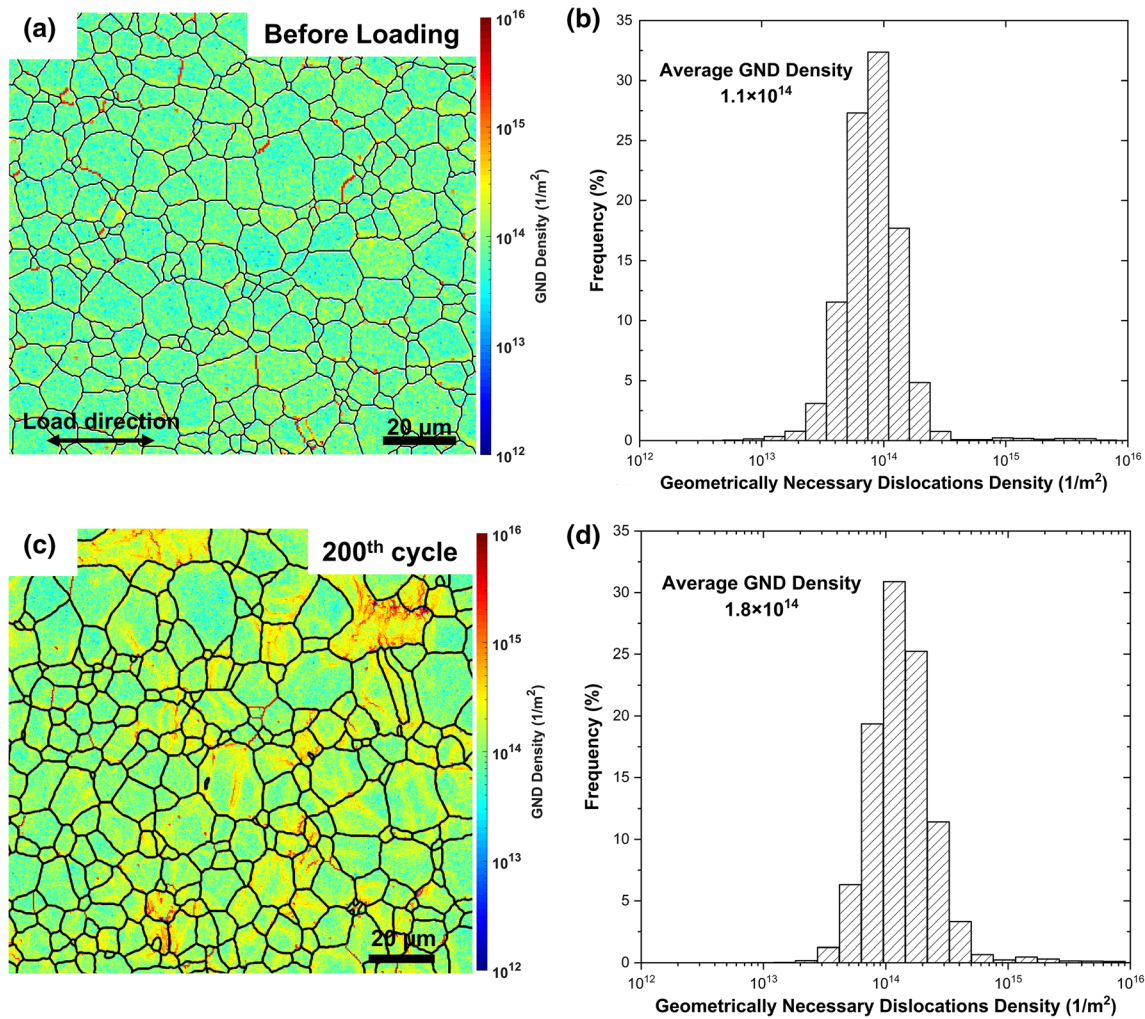
Fig. 11—Geometrically necessary dislocation (GND) density maps with corresponding histograms for the sample: (a) through (b) before loading, and (c) through (d) tested to the 200th cycle.
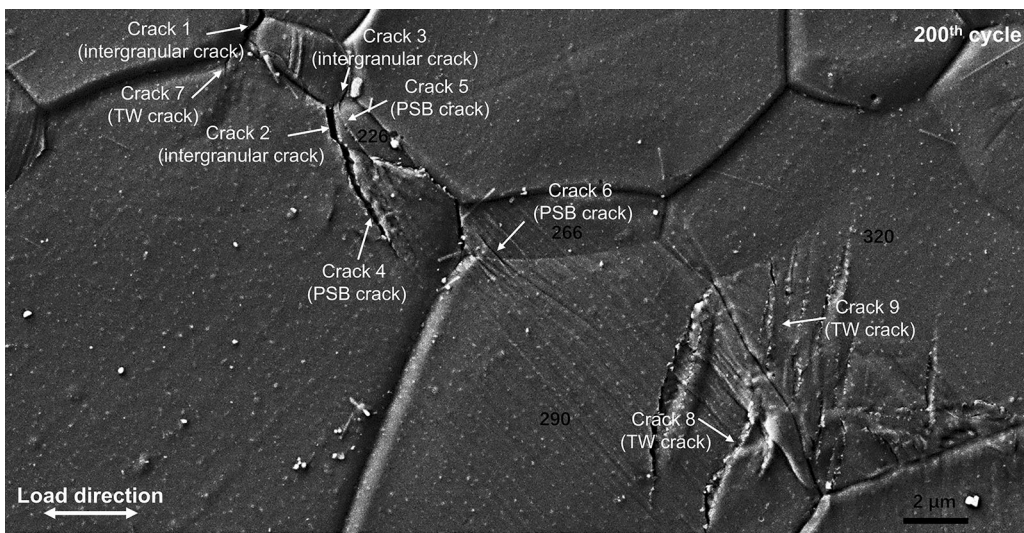


Fig. 12—SE SEM photomicrograph illustrates various types of fatigue crack morphology observed on the sample surface after the 200th cycle.

slip band induced transgranular cracks (PSB cracks, marked by crack 4, 5 and 6), and twin associated transgranular cracks (TW cracks, marked by crack 7, 8 and 9). Note that some intergranular cracks accompanied transgranular cracks (cracks 1 and 2). The transgranular cracks themselves were also closely associated with slip/twinning transfer across grain boundary (cracks 6, 8, and 9). The statistical details of all the observed cracks with their classifications and relative fractions are summarized in Table II.

As shown in Table II, intergranular cracking, with relative frequency of 80.1 pct with respect to the total cracks, was the dominant fatigue damage mechanism, and the representative morphologies observed by high-magnitude SEM images are shown in Figure 13. However, as noted before, the PSB/TW cracks (transgranular cracks) also played an important role in fatigue damage. What's more, some PSB/TW cracks and intergranular cracks were associated. Therefore, we will present and analyze the PSB/TW cracks in detail with special attention paid on their corresponding slip/twinning modes.

Figure 14 illustrates representative PSB cracks with the associated slip systems in three different grains for the sample tested to the 200th cycle (the last cycle). The shaded plane, dashed line, and solid line in the HCP unit cell represents the slip plane ($n$), burgers vector ($b$), and slip trace, respectively. As shown in Figure 14(a), 2nd pyramidal $\langle c + a \rangle$ slip $\left( (\bar{2}112)[2\bar{1}\bar{1}3], m = 0.36 \right)$ induced PSB crack was observed near the grain boundary in grain 240. Similar PSB cracks but induced by

different slip systems were observed in grain 227 (Figure 14(b)) and grain 688 (Figure 14(c)). It is worth to note that some highly localized PSBs developed into cracks, while some of them did not even for the same set of parallel PSBs (formed by the same slip system) in the same grain, indicating heterogeneous deformation. Also note that all the three PSB cracks were associated with other intergranular cracks.

As mentioned before, the EBSD indexing rate was too low due to strain accumulation and we could not identify the twins based on the orientation of deformed sample surface without repolishing. Thus, the active twin variant, which caused the TW cracks, was identified by twinning plane trace analysis. Figure 15 illustrates three representative TW cracks in different grains for the sample tested to the 200th cycle. The active twinning systems are shown in the HCP unit cells with visualized crystallographic orientations located below the figures. The light blue shaded plane, orange dashed line, and orange solid line represents the twinning plane ($K_1$), twinning direction ($\eta_1$), and twinning plane trace, respectively. Note that only absolute values of the Schmid factor $|m|$ are provided here because we failed to determine whether the twins were activated in tensile or compressive loading during the cyclic deformation. As seen in Figure 15(a), TTW $\left( (10\bar{1}2)[\bar{1}011], |m| = 0.49 \right)$ induced TW cracks in grain 103 were observed. Similar TW cracks but induced by different twinning systems were observed in grain 239 (Figure 15(b)) and grain 909 (Figure 15(c)). Note that all the TW cracks were induced by TTW and they commonly exhibited irregular smashed morphology inside the twins.

Figure 16 illustrates representative slip transfer associated transgranular cracks in three different grain pairs for the sample tested to the 200th cycle. As shown in Figure16(a), slip transfer across the grain boundary of grain pair 49–101 was observed, and the corresponding transferred slip systems were basal $\langle a \rangle$-2 $\left( (0001)[\bar{1}2\bar{1}0], m = 0.46 \right)$ and basal $\langle a \rangle$-2 $\left( (0001)[\bar{1}2\bar{1}0], m = 0.44 \right)$ which had $m'$ of 0.84. The transferred PSBs caused two crack pairs connected at the grain boundary, which were PSB crack 1-PSB crack 2 and PSB crack 3-PSB crack 4 as marked in this figure.

### Table II. Summary of Fatigue Crack Classification

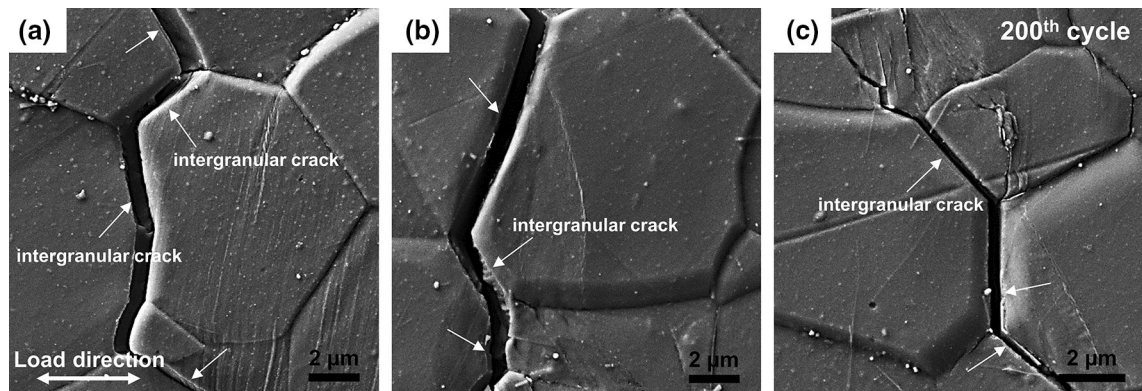| Crack Classification | Proportion |
|---|---|
| Intergranular Crack | 80.1 pct (249) |
| Transgranular Crack | |
| PSB crack | 13.8 pct (43) |
| TW crack | 5.5 pct (17) |
| Other | 0.6 pct (2) |



Fig. 13—High-magnification SE SEM images showing representative intergranular cracks for the sample tested to the 200th cycle at (*a*) through (*c*) different locations.
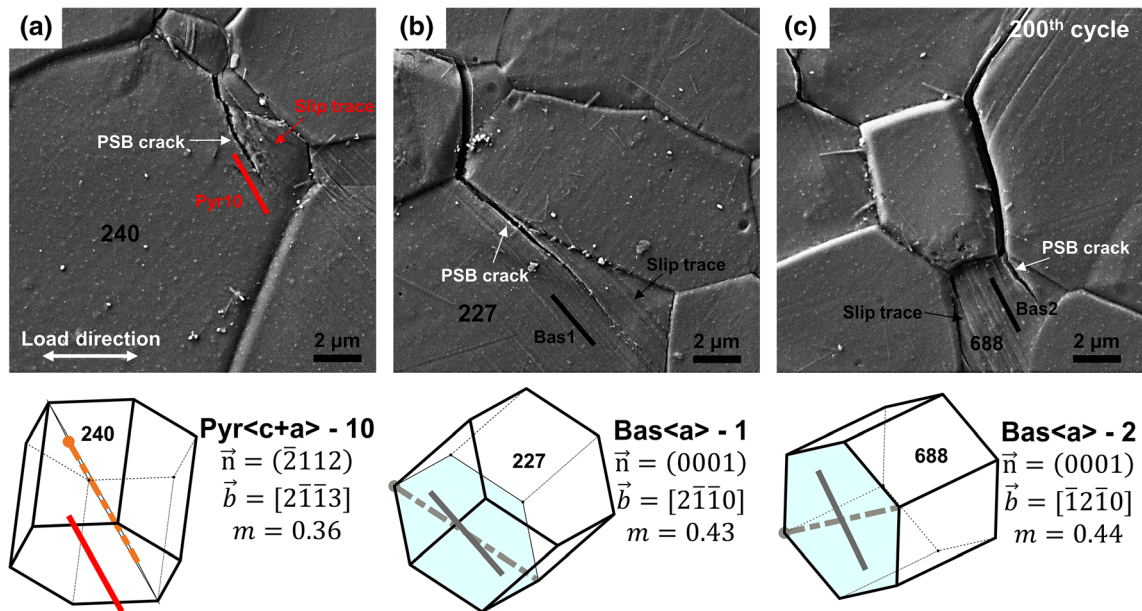
Fig. 14—SE SEM photomicrographs showing representative persistent slip band-associated transgranular cracks (PSB cracks) and the corresponding identified slip systems shown in the HCP unit cells with their crystallographic orientations visualized for the sample tested to the 200th cycle at (*a*) through (*c*) different locations. The slip system and Schmid factor *m* for the observed PSBs are indicated in the images.
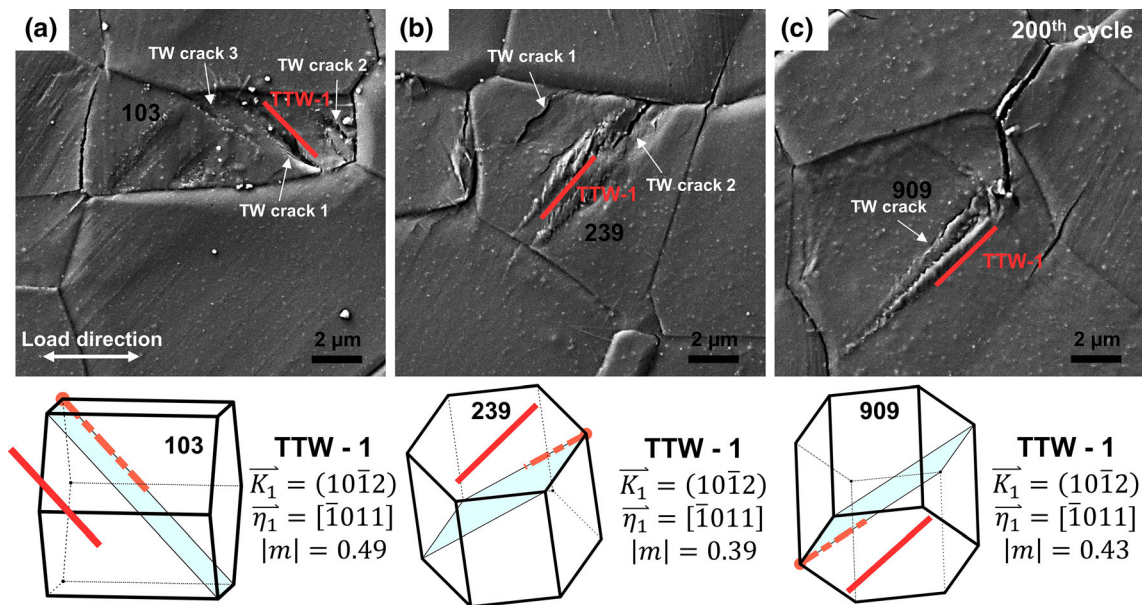


Fig. 15—SE SEM photomicrographs showing representative twin-associated transgranular cracks (TW cracks) and the corresponding identified twinning systems shown in the HCP unit cells with their crystallographic orientations visualized for the sample tested to the 200th cycle at (*a*) through (*c*) different locations. The twinning system and absolute Schmid factor |*m*| for the observed twins are indicated in the images.

Similar cases can be found in Figures 16(b) and (c). It is noteworthy that all the involved transferred slip systems in Figure 16 were the basal ⟨a⟩ slip with both high *m* and *m′* values.

Twinning transfer associated transgranular cracks were also observed, and the only two cases found are shown in Figure 17. As shown in Figure 17(a), twinning transfer across the grain boundary of grain pair 777–796 was observed, and the corresponding transferred twinning systems were TTW-6 $\left((1\bar{1}02)[\bar{1}101], |m| = 0.45\right)$ and TTW-6 $\left((1\bar{1}02)[\bar{1}101], |m| = 0.47\right)$ which had *m′* of 0.96. Note that the transferred TW cracks exhibited smashed morphology inside the twins which was similar to the isolated TW cracks as shown before. A similar case was observed in grain pair 320–290 (Figure 17(b)). The transferred twinning systems exhibited extremely low |*m*| values but relatively high *m′* values.
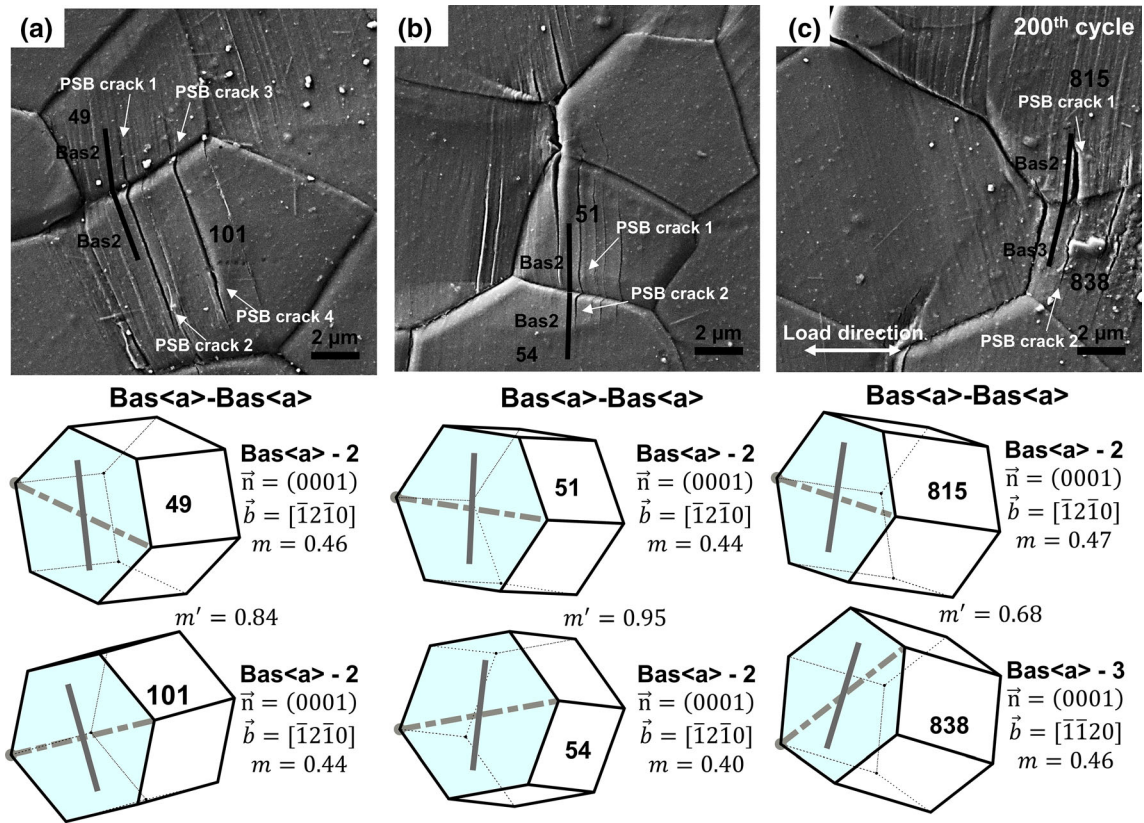
Fig. 16—SE SEM photomicrographs showing representative slip transfer associated transgranular cracks and the corresponding identified slip systems shown in the HCP unit cells with their crystallographic orientations visualized for the sample tested to the 200th cycle at (*a*) through (*c*) different locations. The slip system, Schmid factor *m*, and geometric compatibility parameter *m'* for the observed PSBs are indicated in the images.

### 2. *Correlation between transgranular crack and deformation mode*

As shown before (Figures 14, 15, 16, 17 and Table II), PSB and TW were the two most important crack initiation sites inside grains, which accounted for 69.4 and 27.4 pct of the total transgranular cracks. All the TW cracks were associated with TTWs, while the PSB cracks were initiated from various slip modes. Figure 18(a) summarizes the cracking behavior of different PSBs induced by various slip modes. The PSBs of pyramidal ⟨c + a⟩ slip exhibited the highest cracking fraction of 64.3 pct followed by the basal ⟨a⟩ slip PSBs (~ 35.9 pct), although the basal ⟨a⟩ slip PSB was the dominant PSB. In terms of cracking fraction, it seems that the PSBs induced by the pyramidal ⟨c + a⟩ slip is more likely to crack than that for the basal ⟨a⟩ slip and prismatic ⟨a⟩ slip, and this will be discussed in Section IV–C.

It was also observed that some transgranular cracks were closely related to intergranular cracks (Figures 14(c) and 15(c)) and slip/twinning transfer (Figures 16 and 17). Figure 18(b) illustrates the quantitative statistical results of their relative fractions. More than 60 pct of the PSBs cracks were related to the intergranular cracks, and this fraction for the TW cracks was 29.4 pct, which indicated that the transgranular cracks induced by PSB were more sensitive to intergranular interaction than that for TW cracks. There was 27.9 pct of the PSB cracks which were associated with slip/twinning transfer behavior, and a similar fraction was observed for the TW cracks. In summary, most of the transgranular cracks (PSB cracks (88.4 pct) and TW cracks (58.8 pct)) tended to be accompanied by intergranular cracks and transfer behavior, and did not appear alone.

## IV. DISCUSSION

### A. *The Symmetrical Hysteresis Loops and Underlying Deformation Mechanisms*

The macroscopic stress–strain response of the present Mg-3Y sheet exhibited symmetric hysteresis loops during the cyclic tension-compression LCF (Figure 2). This characteristic is significantly different from that of conventional Mg alloys, *e.g.,* pure Mg,[34] AZ31[35,43] and ZK60[36,44] under similar strain-controlled LCF, which usually exhibited asymmetrical hysteresis loops. Hasegawa *et al.*[45] observed asymmetrical hysteresis loops of extruded AZ31 bar under strain-controlled fatigue tests and proposed a model to evaluate the effect of asymmetry on fatigue life. The model was based on the Manson-Coffin type equation and added the mean stress caused by the asymmetry. According to their
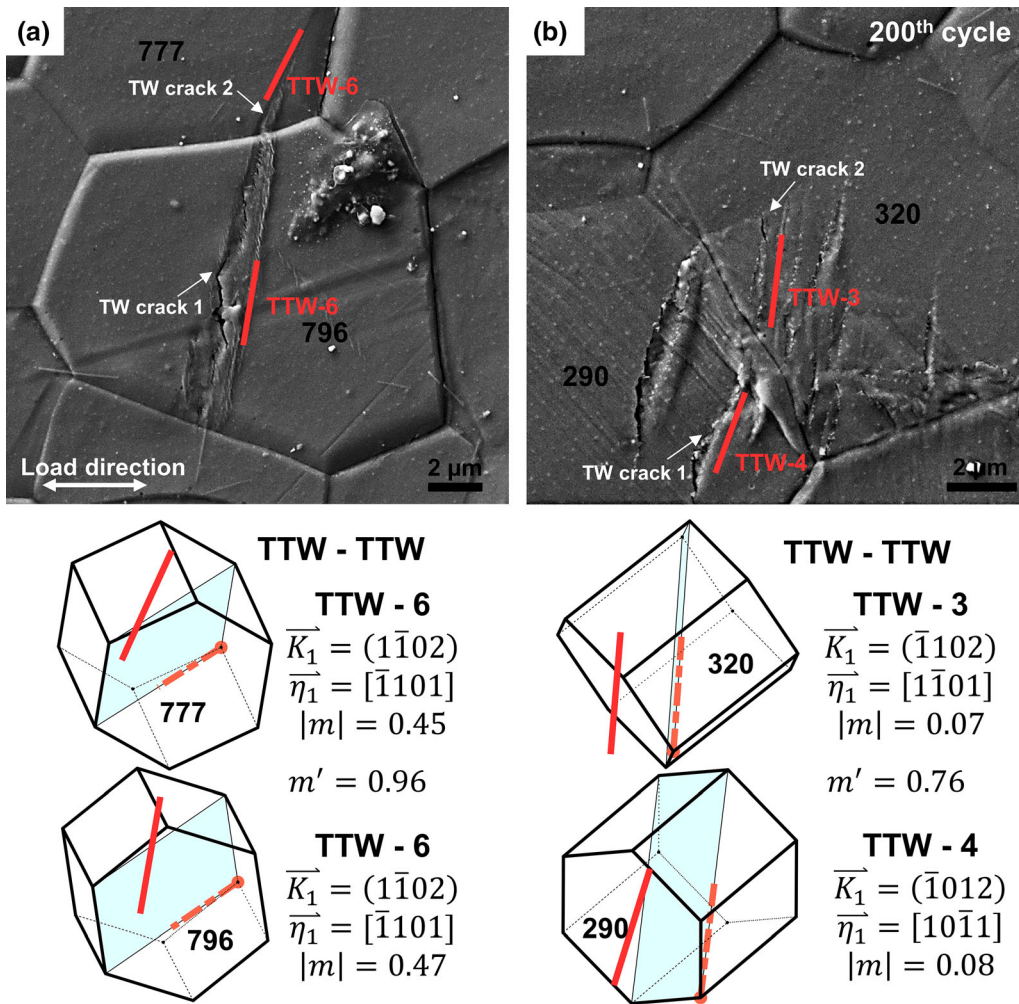
Fig. 17—SE SEM photomicrographs showing representative twinning transfer associated transgranular cracks and the corresponding identified twinning systems shown in the HCP unit cells with their crystallographic orientations visualized for the sample tested to the 200th cycle at (*a*) through (*b*) different locations. The twinning system, absolute Schmid factor |*m*|, and geometric compatibility parameter *m'* for the observed twin pairs are indicated in the images.

work, higher mean stress may result in lower fatigue life, which means more asymmetric behavior will cause a shorter fatigue life. It's well known that the twinning-de-twinning is responsible for the asymmetry in these conventional Mg alloys.[35,36,46,47] Yin *et al.*[35] studied the cyclic deformation behavior of the extruded AZ31 alloy by *in-situ* observation. They observed a large number of twins formed during compression to $\varepsilon_{min}$ and detwinning occurred during unloading and the subsequent tensile loading, which induced the asymmetric hysteresis loops. In summary, two key factors may result in the asymmetric hysteresis loops[45]: one is the strong texture-induced soft orientation for twinning in compression, while hard orientation for twinning and basal slip in tension; the other is that the stresses needed to initiate twinning and activate slip are significantly different. While for the present work, limited TTWs with 0.05 twins per grain and 1.7 pct twin area fraction (Figure 8) were observed. A total of 113 grains (11.4 pct) exhibited distinct slip plane traces for the sample tested to the 200th cycle (Figure 6) and the

slip-dominated deformation were consistent with the concave-down shape of the stress–strain curves (Figure 2). Therefore, the low twinning activity and the dislocation slip-dominated deformation are responsible for the present symmetric hysteresis loops of the Mg-3Y during the LCF test. Similar symmetric hysteresis loops and slip-dominated deformation behavior were also observed in Mg-10Gd-3Y-0.5Zr alloy during a strain-controlled fatigue test.[48]

As indicated in Figure 6(a), basal ⟨a⟩ slip was the dominate slip mode (81.4 pct), and 2nd pyramidal ⟨c + a⟩ slip (12.4 pct) was more than that of prismatic ⟨a⟩ slip (6.2 pct). The non-basal slip activity was enhanced and pyramidal slip exhibited a higher activity. As mentioned in the introduction, limited information about the deformation mechanisms, especially quantitative slip/twinning activity, in Mg alloys during fatigue is available in the literature. Pan *et al.*[21] studied the fatigue mechanism of a cast Mg-8Gd-3Y-Zr alloy during stress-controlled HCF, and only basal slip traces were observed and the basal slip induced PSMs were believed
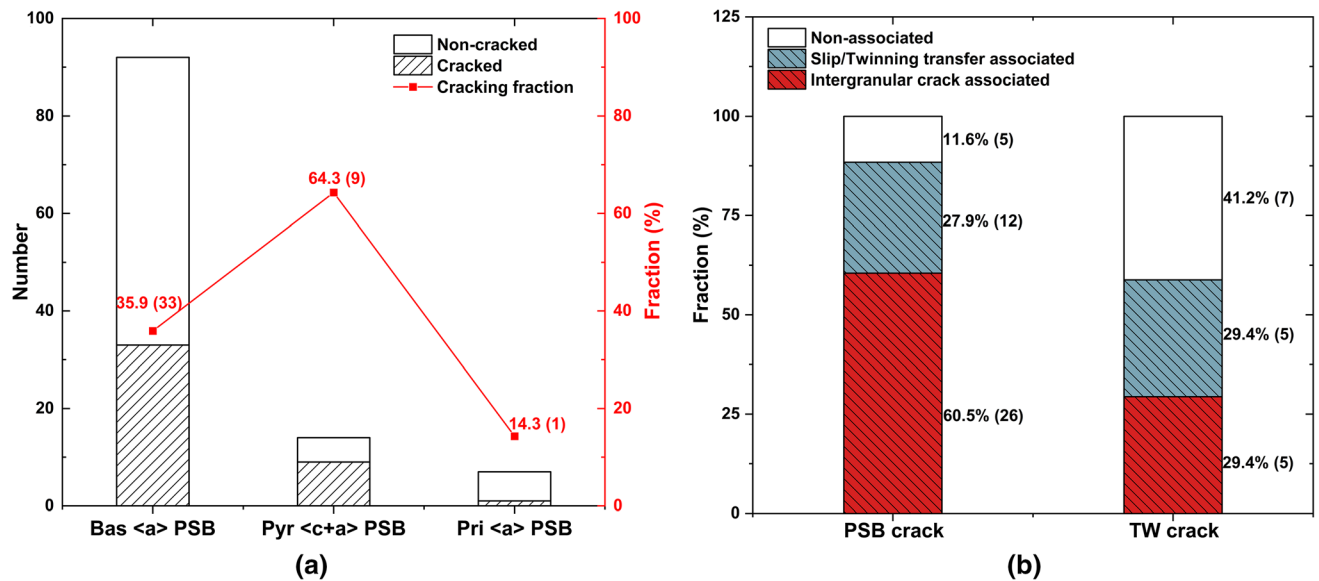
Fig. 18—(a) The cracking behavior of different PSBs induced by various slip modes. The cracking fraction for a particular PSB crack is the ratio of cracked PSB number and total PSB number. The number of the observed PSBs is also provided in parentheses. (b) Relationship between transgranular cracks and intergranular cracks and slip/twinning transfer.

as the predominant damage mechanism. He et al.[49] investigated the HCF behavior of an extruded Mg-10Gd-3Y-0.5Zr alloy, and they found that only basal slip was active and fatigue crack initiated from the basal PSBs. The deformation mechanisms of the above two alloys are significantly different with the present work, although they are all Mg-RE-based alloys. It seems that the slip activity of Mg alloys during fatigue deformation needs further study. However, the slip activity identified in the present work for the Mg-3Y alloy is generally consistent with that obtained from quasi-static loading for Mg-Y-based alloys.[18,19,31] For example, Long et al.[18] investigated the effects of Y contents on the slip/twinning activity in Mg-Y alloys during compression and suggested that the Y addition can significantly enhance non-basal slips, especially for the pyramidal $\langle c + a \rangle$ slips, and depress twinning. Thus, it seems that the effect of Y addition to Mg on the slip activity for the quasi-static uniaxial loading and dynamic cyclic loading is quite similar. To date, several mechanisms have been proposed to explain the enhanced pyramidal slip by Y additions. Sandlöbes et al.[50, 51] observed pronounced pyramidal $\langle c + a \rangle$ slip and intrinsic stacking fault $I_1$ in the Mg-Y alloys by TEM observation, and proposed that the Y addition increased $\langle c + a \rangle$ dislocations nucleation by the stacking fault. Wu et al.[52] proposed that the RE solutes, such as Y, can decrease the harmful pyramidal-to-basal transition which will cause immobile dislocations, and consequently increase the $\langle c + a \rangle$ dislocation mobility.

## B. The Intergranular Cracking

In this study, the fatigue damage on the specimen surface after cyclic loading was usually observed at grain boundaries, PSBs, and twins. Intergranular cracking

was the dominant cracking mode accounted for 80.1 pct of the total cracks observed (Table II). What's more, the intergranular cracks were closely related to the transgranular cracks (Figures 14, 15, and 16).

Intergranular cracking as the primary cracking mode during fatigue was reported in other Mg alloys.[53–58] Wu et al.[53] studied the LCF behavior of Mg-10Gd-2.0Y-0.46Zr alloy at 573K, and they found that intergranular cracks dominated the cracking behavior at lower strain amplitudes (0.3 and 0.45 pct). Marrow et al.[54] studied the environment-assisted cracking behavior of WE43 cast alloys in the T6 peak-aged condition at room temperature, and they also reported that the intergranular cracking was primary.

However, Yue et al.[20] studied the HCF behavior of NZ30K alloy at room temperature. They did not observe any intergranular cracks. Instead, PSB (transgranular) cracks dominated the cracking behavior. Similar results were also reported.[21,49] Thus, the cracking behavior (competition of inter- and transgranular cracking) during fatigue is complex and may be affected by alloy composition, microstructure, and loading condition.

## C. The Transgranular Cracking and Active Slip/Twinning Modes

Although transgranular cracking was not the predominant cracking mode for the present study, it still contributed about ~ 20 pct of the total cracks observed (Table II). As noted, the transgranular cracks were closely related to the PSBs and twins which induced by various slip modes and TTW variants (Figures 14, 15, and 16).

In this study, we observed 113 PSBs and 84 twins after 200 cycles LCF deformation. The cracking fractions of PSBs and twins were 38.1 and 20.2 pct, respectively. This implies that the PSBs were easier to crack than that of twins, which is consistent with the study of the LCF of GW123K at room temperature.[59]

All the TW cracks were associated with the same twin mode of TTW, but the PSB cracks were related to various slip modes (Figures 14, 16, and 18). Although the basal $\langle a \rangle$ slip PSB was the dominant PSB, the corresponding crack fraction was 35.9 pct, which was the second rank (Figure 18(a)). It is interesting to note that the largest cracking fraction (64.3 pct) belonged to the pyramidal $\langle c + a \rangle$ slip PSB, which was 1.8 times larger than that of basal $\langle a \rangle$ slip PSB. It indicated that the PSBs induced by the pyramidal $\langle c + a \rangle$ slip was more likely to crack than that for the basal $\langle a \rangle$ slip and prismatic $\langle a \rangle$ slip. It is worth to note that large proportion of the active pyramidal $\langle c + a \rangle$ slips exhibited low Schmid factors in terms of both $m$ and $m_{nor}$, as shown in Figure 6. For the pyramidal $\langle c + a \rangle$ slip, 42.9 pct of the $m_{nor}$ values were below 0.25 and 28.6 pct of them were below 0.1. Note that the Schmid factor used here is totally geometric, which were calculated assuming that the local (grain scale) stress was equivalent to the globally applied stress. Thus, the significant number of the active pyramidal $\langle c + a \rangle$ slip with small Schmid factors implied that local stress concentration played a critical role in their activations. This viewpoint is somewhat supported by the IGM and GND density distributions shown in Figures 10 and 11, which showed that significantly heterogeneous plastic deformation developed during the LCF indicating local stress of some areas might deviate from the global stress. Thus, it is reasonable to conclude the high cracking fraction of the pyramidal $\langle c + a \rangle$ slip PSBs is caused by the local stress concentration which is necessary for its activation because of its relatively large critical resolved shear stress (CRSS).[60–62]

Wang et al.[63] reported that fatigue cracks were more likely to initiate on the prismatic $\langle a \rangle$ PSBs in an extruded AZ31B alloy during a fully reversed strain-controlled tension-compression fatigue with a twin volume fraction of 60 pct at low strain amplitudes. However, Pan et al.[21] reported that the basal $\langle a \rangle$ slip PSBs was the dominant fatigue damage mechanism in Mg-8Gd-3Y-Zr (wt pct) alloy during HCF. These studies indicate that the dominant cracked PSBs induced by various slip modes may be influenced by load conditions, alloy composition, and microstructure. Although it is well accepted that PSB is a critical fatigue damage site,[64–66] our current understanding of the relationship of PSB crack and the corresponding active slip modes is rather limited, and it deserves further investigation in detail.

## V. CONCLUSION

The grain-scale slip/twinning activity and cracking behavior for an extruded Mg-3Y sheet during 1 pct strain-controlled tension-compression LCF along the extruded direction at room temperature were investigated quantitatively by slip trace analysis and EBSD-based misorientation analysis. The main conclusions are drawn as follows:

(1) The fatigue failure cycle was identified to be 200 cycle. The samples exhibited symmetric hysteresis loops with zero mean stress during cyclic deformation.

(2) The contribution for the deformation of twinning was limited, and only tension twins with area fraction of 1.7 pct were observed. Among 989 grains analyzed, 11.4 pct (113) grains exhibited observable slip traces. Basal $\langle a \rangle$ slip was the dominant slip mode (81.4 pct), and the pyramidal II slip (12.4 pct) also exhibited high activity. The slip-dominated deformation behavior was responsible for the symmetric hysteresis loops.

(3) Among the total 311 cracks observed for the 200th cycle, 80.1 pct were intergranular cracks and 19.9 pct were transgranular cracks. PSB (13.8 pct) and TW (5.5 pct) were the two key transgranular crack initiation sites. Transgranular cracks associated with slip/twinning transfer were also occasionally observed.

(4) The cracking fraction (cracked PSBs/total PSBs) for various PSBs induced by different slip modes followed pyramidal II (64 pct) > basal (36 pct) > prismatic (14 pct). Strain localization was likely to be responsible for the high cracking fraction for pyramidal II PSBs, which was consistent with the small normalized Schmid factors and the heterogeneous distribution of geometrically necessary dislocation density.

(5) About 50 pct (31) transgranular cracks were related to the appearance of intergranular cracks. The correlation between intergranular cracks and PSB cracks was more susceptible (60.5 pct) than that of TW cracks (29.4 pct).

## REFERENCES

1. B.L. Mordike and T. Ebert: *Mat. Sci. Eng. A*, 2001, vol. 302, pp. 37–45.
2. R. Narayanasamy, S. Sathiyanarayanan, and R. Ponalagusamy: *J. Mater. Process. Technol.*, 2000, vol. 102, pp. 56–58.

3. K.F. Zhang, D.L. Yin, and D.Z. Wu: *Int. J. Mach. Tool. Manu.*, 2006, vol. 46, pp. 1276–80.
4. B. Wang, R. Xin, G. Huang, and Q. Liu: *Mat. Sci. Eng. A*, 2012, vol. 534, pp. 588–93.
5. L. Helis, K. Okayasu, and H. Fukutomi: *Mat. Sci. Eng. A*, 2006, vol. 430, pp. 98–103.
6. S. Chen, L. Zheng, S. Zhang, H. Song, and M. Cheng: *Acta Metall. Sin. (Engl. Lett.)*, 2015, vol. 28, pp. 1426–34.
7. A. Gryguc, S.K. Shaha, S.B. Behravesh, H. Jahed, M. Wells, B. Williams, and X. Su: *Int. J. Fatigue*, 2017, vol. 104, pp. 136–49.
8. S. Suresh: *Fatigue of Materials*, 2nd ed., Cambridge UP, New York, NY, 2003, pp. 1–679.
9. S.R. Agnew and Ö. Duygulu: *Int. J. Plast.*, 2005, vol. 21, pp. 1161–93.
10. S.R. Agnew, C.N. Tomé, D.W. Brown, T.M. Holden, and S.C. Vogel: *Scr. Mater.*, 2003, vol. 48, pp. 1003–08.
11. M.H. Yoo: *Metall. Mater. Trans. A*, 1981, vol. 12A, pp. 409–18.
12. N. Stanford: *Philos. Mag. Lett.*, 2008, vol. 88, pp. 379–86.
13. S.A. Farzadfar, E. Martin, M. Sanjari, E. Essadiqi, S. Yue, and E.E.S. Yue: *J. Mater. Sci.*, 2012, vol. 47, pp. 5488–5500.
14. Z.R. Zeng, Y.M. Zhu, S.W. Xu, M.Z. Bian, N. Birbilis, J.F. Nie, and C.H.J. Davies: *Acta Mater.*, 2016, vol. 105, pp. 479–94.
15. S.A. Habib, A.S. Khan, T. Gnäupel-Herold, J.T. Lloyd, and S.E. Schoenfeld: *Int. J. Plast.*, 2017, vol. 95, pp. 163–90.
16. J.W. Lu, D.D. Yin, G.H. Huang, G.F. Quan, Y. Zeng, H. Zhou, and Q.D. Wang: *Mat. Sci. Eng. A*, 2017, vol. 700, pp. 596–608.
17. D. Zhang, H. Wen, M.A. Kumar, F. Chen, L. Zhang, I.J. Beyerlein, J.M. Schoenung, S. Mahajan, and E.J. Lavernia: *Acta Mater.*, 2016, vol. 120, pp. 75–85.
18. L.J. Long, G.H. Huang, D.D. Yin, B. Ji, H. Zhou, and Q.D. Wang: *Metall. Mater. Trans. A*, 2020, vol. 51A, pp. 2738–51.
19. S. Sandlöbes, M. Friák, S. Zaefferer, A. Dick, S. Yi, D. Letzig, Z. Pei, L.F. Zhu, J. Neugebauer, and D. Raabe: *Acta Mater.*, 2012, vol. 60, pp. 3011–21.
20. H. Yue, P. Fu, L. Peng, Z. Li, J. Pan, and W. Ding: *Mater. Charact.*, 2016, vol. 111, pp. 93–105.
21. J. Pan, P. Fu, L. Peng, B. Hu, H. Zhang, and A.A. Luo: *Int. J. Fatigue*, 2018, vol. 118, pp. 104–16.
22. H. Bayani and E. Saebnoori: *J. Rare Earths*, 2009, vol. 27, pp. 255–58.
23. A.K. Ray and D.S. Wilkinson: *Mat. Sci. Eng. A*, 2016, vol. 658, pp. 33–41.
24. Q. Huo, D. Ando, Y. Sutou, and J. Koike: *Mat. Sci. Eng. A*, 2016, vol. 678, pp. 235–42.
25. S. Sandlöbes, S. Zaefferer, I. Schestakow, S. Yi, and R. Gonzalez-Martinez: *Acta Mater.*, 2011, vol. 59, pp. 429–39.
26. G.H. Huang, D.D. Yin, J.W. Lu, H. Zhou, Y. Zeng, G.F. Quan, and Q.D. Wang: *Mat. Sci. Eng. A*, 2018, vol. 720, pp. 24–35.
27. F. Wang, J. Dong, Y. Jiang, and W. Ding: *Mat. Sci. Eng. A*, 2013, vol. 561, pp. 403–10.
28. R. Hielscher, C.B. Silbermann, E. Schmidl, and J. Ihlemann: *J. Appl. Crystallogr.*, 2019, vol. 52, pp. 984–96.
29. F. Bachmann, R. Hielscher, and H. Schaeben: *Solid State Phenom.*, 2010, vol. 160, pp. 63–68.
30. H. Wang, C.J. Boehlert, Q.D. Wang, D.D. Yin, and W.J. Ding: *Int. J. Plast.*, 2016, vol. 84, pp. 225–76.
31. D.D. Yin, Q.D. Wang, C.J. Boehlert, Z. Chen, H.M. Li, R.K. Mishra, and A. Chakkedath: *Metall. Mater. Trans. A*, 2016, vol. 47A, pp. 6438–52.
32. C.J. Boehlert, Z. Chen, I. Gutiérrez-Urrutia, J. Llorca, and M.T. Pérez-Prado: *Acta Mater.*, 2012, vol. 60, pp. 1889–1904.
33. D.M. Li, K.W. Kim, and C.S. Lee: *Int. J. Fatigue*, 1997, vol. 19, pp. 607–12.
34. A.D. Murphy-Leonard, D.C. Pagan, A. Beaudoin, M.P. Miller, and J.E. Allison: *Int. J. Fatigue*, 2019, vol. 125, pp. 314–23.
35. S.M. Yin, H.J. Yang, S.X. Li, S.D. Wu, and F. Yang: *Scr. Mater.*, 2008, vol. 58, pp. 751–54.
36. S. Dong, Q. Yu, Y. Jiang, J. Dong, F. Wang, L. Jin, and W. Ding: *Int. J. Plast.*, 2016, vol. 91, pp. 25–47.
37. A. Gryguc, S.B. Behravesh, S.K. Shaha, H. Jahed, M. Wells, B. Williams, and X. Su: *Int. J. Fatigue*, 2018, vol. 116, pp. 429–38.
38. Z. Wu, R. Ahmad, B. Yin, S. Sandlöbes, and W.A. Curtin: *Science*, 2018, vol. 359, pp. 447–52.
39. T.C. Lee, I.M. Robertson, and H.K. Birnbaum: *Metall. Trans. A*, 1990, vol. 21A, pp. 2437–47.
40. T.R. Bieler, P. Eisenlohr, F. Roters, D. Kumar, D.E. Mason, M.A. Crimp, and D. Raabe: *Int. J. Plast.*, 2009, vol. 25, pp. 1655–83.
41. N. Allain-Bonasso, F. Wagner, S. Berbenni, and D.P. Field: *Mat. Sci. Eng. A*, 2012, vol. 548, pp. 56–63.
42. W. Pantleon: *Scr. Mater.*, 2008, vol. 58, pp. 994–97.
43. J. Klemenc, D. Šeruga, A. Nagode, and M. Nagode: *Materials*, 2019, vol. 12, p. 3692.
44. Y. Xiong, X. Gong, and Y. Jiang: *Fatigue Fract. Eng. Mater. Struct.*, 2018, vol. 41, pp. 1504–13.
45. S. Hasegawa, Y. Tsuchida, H. Yano, and M. Matsui: *Int. J. Fatigue*, 2007, vol. 29, pp. 1839–45.
46. L. Wu, S.R. Agnew, Y. Ren, D.W. Brown, B. Clausen, G.M. Stoica, H.R. Wenk, and P.K. Liaw: *Mat. Sci. Eng. A*, 2010, vol. 527, pp. 7057–67.
47. J.B. Jordon, J.B. Gibson, M.F. Horstemeyer, H.E. Kadiri, J.C. Baird, and A.A. Luo: *Mat. Sci. Eng. A*, 2011, vol. 528, pp. 6860–71.
48. F.A. Mirza, D.L. Chen, D.J. Li, and X.Q. Zeng: *Mat. Sci. Eng. A*, 2013, vol. 575, pp. 65–73.
49. C. He, X. Shao, S. Yuan, L. Peng, Y. Wu, Q. Wang, and Q. Chen: *Mat. Sci. Eng. A*, 2019, vol. 774, pp. 716–23.
50. S. Sandlöbes, Z. Pei, M. Friák, L.F. Zhu, F. Wang, S. Zaefferer, D. Raabe, and J. Neugebauer: *Acta Mater.*, 2014, vol. 70, pp. 92–104.
51. S. Sandlöbes, M. Friák, J. Neugebauer, and D. Raabe: *Mat. Sci. Eng. A*, 2013, vol. 576, pp. 61–68.
52. Z. Wu and W.A. Curtin: *Nature*, 2015, vol. 526, pp. 62–67.
53. L. Wu, Z. Yang, W. Xia, Z. Chen, and L. Yang: *Mater. Des.*, 2012, vol. 36, pp. 47–53.
54. T.J. Marrow, A. BinAhmad, I.N. Khan, S.M.A. Sim, and S. Torkamani: *Mat. Sci. Eng. A*, 2004, vols. 387–389, pp. 419–23.
55. Y. Xiong: *Mat. Sci. Eng. A*, 2016, vol. 675, pp. 171–80.
56. Y. Li, S. Qiu, Z. Zhu, D. Han, J. Chen, and H. Chen: *Int. J. Fatigue*, 2017, vol. 100, pp. 105–12.
57. Y. Xiong and Y. Jiang: *Mat. Sci. Eng. A*, 2016, vol. 677, pp. 58–67.
58. Q. Yu, J. Zhang, and Y. Jiang: *Mat. Sci. Eng. A*, 2011, vol. 528, pp. 7816–26.
59. S.M. Yin and S.X. Li: *J. Mater. Sci. Technol.*, 2013, vol. 29, pp. 775–80.
60. Q. Ma, B. Li, Z. Mcclelland, and S.J. Horstemeyer: *Metall. Mater. Trans. A*, 2013, vol. 44, pp. 4480–85.
61. Q. Ma, B. Li, W.R. Whittington, A.L. Oppedal, P.T. Wang, and M.F. Horstemeyer: *Acta Mater.*, 2014, vol. 67, pp. 102–15.
62. A. Khosravani, J. Scott, M.P. Miles, D. Fullwood, B.L. Adams, and R.K. Mishra: *Int. J. Plast.*, 2013, vol. 45, pp. 160–73.
63. F. Wang, M. Liu, J. Sun, M. Feng, L. Jin, J. Dong, and Y. Jiang: *Mater. Charact.*, 2019, vol. 149, pp. 118–23.
64. B. Wen, F. Wang, L. Jin, and J. Dong: *Mat. Sci. Eng. A*, 2016, vol. 667, pp. 171–78.
65. Y. Takahashi, H. Yoshitake, R. Nakamichi, T. Wada, M. Takuma, T. Shikama, and H. Noguchi: *Mat. Sci. Eng. A*, 2014, vol. 614, pp. 243–49.
66. H. Wu, S. Hamada, and H. Noguchi: *Int. J. Fatigue*, 2014, vol. 63, pp. 1–11.